Effect of tectonic inversion on supra-salt fault geometry and reactivation histories in the Southern North Sea

Abubakar Maunde[a, b, *], Tiago M. Alves[a]

[a] 3D Seismic Lab, School of Earth and Environmental Sciences, Cardiff University, Main Building, Park Place, Cardiff, CF10 3AT, United Kingdom

[b] Geology Department, School of Physical Sciences, Modibbo Adama University, P.M.B 2076, Yola, Nigeria

***Corresponding author**: E-mail: abubakarmaunde@mautech.edu.ng; maundea@cardiff.ac.uk. Telephone: +2348161358265; +447778942870

Abstract

High-resolution 3D seismic and borehole data in the Broad Fourteens Basin, Southern North Sea, are used to investigate the relationship between lithology and fault throw distribution, as well as to understand the reactivation and growth histories of faults developed due to tectonic inversion. Two (2) distinct tiers of faults are identified, and their geometry analysed in detail. Tier 1 faults comprise closely spaced sets of normal faults that resulted from the progressive buckling and stretching of Upper Mesozoic strata during Late Cretaceous to Paleogene tectonic inversion. They have been reactivated but still show net normal throw separations, even though they were formed during a period of regional compression. Tier 2 faults comprise densely spaced sets of normal faults in Paleogene strata with a broad range of strikes, forming a polygonal pattern. These faults relate to early diagenesis but still record the effect of the Paleogene inversion episode. An important characteristic is that Tier 1 faults are highly segmented and show differences in throw distribution between shale-rich and sandy intervals. The faults are more segmented, with relatively small throw maxima of 14 ms (17.7 m) in shale-

rich intervals, while sandy intervals are less segmented with larger throw maxima of 32 ms (40.3 m). Discrepancies in fault throw distribution and segmentation increase the chances of compartmentalisation or localised fluid flow through fault linkages, presenting at the same time significant risks when injecting CO_2 in subsurface traps. Recognising the effect of tectonic inversion on supra-salt fault geometry, and reactivation histories, can be crucial to the characterisation of faulted hydrocarbon and carbon capture and storage (CCS) reservoirs in tectonically inverted basins such as the Southern North Sea.

Keywords: Southern North Sea; Tectonic shortening; Mechanical stratigraphy; Lithology; Fault throw; Fault reactivation; Fault linkage.

1. Introduction

In layered successions, the mechanical stratigraphy of the host rock affects the nucleation, segmentation, geometry, and displacement distribution of tectonic faults (Peacock and Sanderson, 1991; Mansfield and Cartwright, 1996; Gross et al. 1997; Childs et al. 2009; Gabrielsen et al., 2016; Ferrill et al. 2017). This means that faults tend to localise (and be less segmented) in harder lithologies such as limestone and sandstone, while becoming more widely distributed (and segmented) in weaker lithologies such as claystone and shale (Schöpfer et al., 2006; Libak et al., 2019). In parallel, analogue deformation experiments show that weak intervals can act as detachments that cause stress decoupling at a local scale, preventing the propagation of faults across specific intervals. This results in a preferable horizontal propagation of faults to the detriment of their vertical growth (Bahroudi et al., 2003; Withjack and Callaway 2000; Richardson et al., 2005; Gabrielsen et al., 2016). Such a horizontal shift in fault geometry across an incompetent layer can result in vertical fault segmentation whereby

fault segments are hard- or soft-linked (Bahroudi et al. 2003; Mansfield and Cartwright, 1996; Maunde et al., 2021).

Late Cretaceous to Paleogene tectonic inversion in the Broad Fourteens Basin, Southern North Sea, contributed to the generation, and subsequent reactivation, of normal faults in supra-salt overburden rocks (Oudmayer and De Jager, 1993; Nalpas et al., 1995; Gerling et al., 1999; Wong et al., 2001; van Verweij and Simmelink, 2002; De Lugt et al., 2003; 2002; Duin et al., 2006). Broad anticlines with outer-arc normal faults were formed in response to the Alpine inversion episodes affecting this part of NW Europe: the Sub-Hercynian, Laramide, Pyrenean and Savian tectonic episodes. This had mostly a positive economic impact, as tectonic movements reactivated older faults and allowed the secondary migration of hydrocarbons into shallower reservoir units (Van Balen et al., 2000; Isaksen, 2004). Nevertheless, to understand the effect of tectonic inversion on the geometry and reactivation histories of faults in the Southern North Sea is key, as these structures add structural complexity to supra-salt reservoir units. Active fracturing provides a pathway for fluids where distinct fault segments interact, with the loci of fault segment linkage across seal units increasing the permeability of host rocks, thus allowing the migration of fluid out of underlying reservoirs (Curewitz and Karson, 1997; Knai and Knipe 1998). Conversely, faults can compartmentalise reservoir units where they form barriers to fluid flow, a character resulting in increasing exploration costs as more wells are needed to retrieve hydrocarbons, or store CO_2 and other gases (Hardman and Booth, 1991; Caine et al. 1996; Cartwright et al., 2007; Bentham et al., 2013).

Using 3D seismic and well data, this paper explores the relationship amongst lithology, displacement distribution and the reactivation histories of Upper Mesozoic supra-salt faults in the Broad Fourteens Basin, Southern North Sea (Fig. 1a). The aims of this paper relate to the fact that hydrocarbon traps are much more likely to leak during periods of fault reactivation than when the faults are inactive, all other parameters of seal integrity being the same (Caine

et al. 1996; Hooper, 1991; Gartrell et al., 2002; Wiprut and Zoback, 2000, 2002; Cartwright et al., 2007; Bentham et al., 2013; Ward et al., 2016). Hence, this work aims to address the following questions:

a) What are the geometry and reactivation styles of faults developing during tectonic shortening?
b) What mode(s) of fault propagation and growth are observed in successions presenting differing lithologies?
c) What is the effect on reservoirs and seal intervals of faults reactivating during tectonic shortening?

2. Data and methods

2.1. Data

Three-dimensional (3D) seismic and borehole data from the Broad Fourteens Basin, Southern North Sea, are used in this work. The data were acquired in the northern end of the Broad Fourteens Basin, offshore The Netherlands, between 53.1° - 53.3°N and 3.8° - 4.2°E. The interpreted seismic volume covers an area of about 845 km^2 at a shallow water depth of 37.7 m (Fig. 1a).

The seismic data are stacked with a 2 ms vertical sampling interval, and a 25 x 25 m bin size, providing a maximum horizontal resolution of 25 m. The resulting seismic volume is zero-phase time migrated and displayed with a normal positive polarity so that an increase in acoustic impedance is represented by a peak (red seismic reflection). A decrease in acoustic impedance is represented by a trough, i.e. a black seismic reflection (SEG European Convention; Brown, 2003). The vertical scale of the seismic data is in two-way travel time (TWTT), up to a recording length of about 4.0 seconds.

97 *2.2. Methods*

98 Seismic horizons and faults were mapped using Schlumberger's Petrel®. First, we mapped
99 seven seismic units (Units S1 to S7) bounded by Upper Carboniferous to Miocene
100 unconformities, and tied them to well stratigraphic information published in Penge et al. (1999)
101 and van Verweij and Simmelink (2002) (Fig. 3). We then imaged and interpreted listric faults,
102 and two distinct tiers of normal faults, in Upper Mesozoic to Paleogene strata. Throw data (T)
103 for the interpreted faults were acquired by measuring differences between footwall and
104 hanging-wall horizon cut-offs (Fig. 2a). These measurements were taken along the fault planes
105 on seismic profiles perpendicular, and also oblique, to local fault strike, bearing in mind local
106 changes in fault geometry and strike.

107 Two-dimensional (2D) contour maps and throw-depth (T-Z) profiles were produced to assess
108 the reactivation and vertical growth styles of faults. From the 2D contour maps, throw-distance
109 (T-X) profiles were produced to assess fault growth histories and the role of lithology on fault
110 throw distribution. The measured fault throw values were depth converted from seconds to
111 meters using Equation (1) below.

112 $$V = \frac{2Z}{T} \quad (1)$$

113 where (V) is the interval or average velocity in m/s, (Z) is the depth in meters, and (T) is the
114 two-way travel time in seconds, gathered from borehole data.

115 The vertical seismic resolution for the target intervals in Upper Mesozoic strata is 15.8 m based
116 on a dominant frequency of 40 Hz and an average velocity of 2521.3 m/s. As fault-throw
117 measurements depend on the vertical sampling interval, rather than the vertical seismic
118 resolution (Tao and Alves, 2019), the minimum fault offset resolved on-screen during fault
119 throw analysis varies from 2 ms (1.9 m) to 3 ms (3.8 m). However, uncertainty in the positions

of stratal terminations does introduce a minimal error associated with the relative depth of the recorded fault throws (Fig. 2). This is a function of the frequency content of the seismic dataset (Mansfield and Cartwright, 1996). Errors associated with spurious velocity estimates may also affect the throw values when converted to meters. These limitations will affect the absolute value of estimated fault throws.

Throw-depth (T-Z) profiles can offer information on multiple parameters such as fault nucleation, growth, segmentation, linkage of individual faults and rock competence (Baudon and Cartwright, 2008; Peacock and Sanderson, 1991; Maunde et al., 2021). Discrepancies in throw gradients often result from mechanical heterogeneities, fault reactivation and fault segmentation (Childs et al., 1996; Baudon and Cartwright, 2008; Laubach et al., 2009). Therefore, our throw-depth (T-Z) analyses aimed to identify fault throw anomalies which will, in this paper, be linked to rock properties and local mechanical stratigraphy.

3. Geological and seismic-stratigraphic settings

The Broad Fourteens Basin, part of the larger South Permian Basin, records a complex history of rifting, halokinesis and tectonic inversion (Duin et al., 2006; Nalpas et al., 1995; Van Wijhe, 1987; Verweij and Simmelink, 2002; Ziegler, 1990). The basin contains Upper Paleozoic and Mesozoic strata overlain by Cenozoic siliciclastics (Van Wijhe, 1987; Van Adrichem Boogaert and Kouwe, 1993; Gerling et al., 1999; van Verweij and Simmelink, 2002). Structural styles in the Broad Fourteens Basin are dominated by normal faulting, which reflects the predominance of an extensional regime since the Late Paleozoic (Fig. 4). Minor reverse movement is observed along only a few normal faults (Alves and Elliott, 2014) (Fig. 4).

3.1. Upper Paleozoic

144 Towards the end of the Carboniferous a large foreland basin, the Variscan Foreland Basin, was
145 formed in what is now the Southern North Sea (Duin et al., 2006; Oudmayer and De Jager,
146 1993; Van Wijhe, 1987; Ziegler, 1990). Thick lacustrine and deltaic intervals with interbedded
147 coal seams were deposited at this time as part of the Limburg Group (Fig. 3). Included in this
148 unit are the Westphalian Coal Measures, a major source of gas in Northern Europe (Gerling et
149 al., 1999; Van Wijhe, 1987). Oblique-slip normal faulting predominated after the Variscan
150 Orogeny, with the largest faults cutting through the Variscan fold belt and propagating along
151 older NW-SE trending basement faults. In fact, the present-day structural grain of the Southern
152 North Sea follows horst-and-graben structures bounded by the latter basement faults (Duin et
153 al., 2006; Oudmayer and De Jager, 1993; Van Wijhe, 1987; Ziegler, 1990).

154 Sedimentation in the Permian was interrupted by thermal upwelling induced by doleritic
155 magma, which intruded the basement through oblique-slip dextral normal faults. This hiatus is
156 expressed in the form of a Saalian unconformity separating Lower from Upper Rotliegend
157 strata (Van Wees et al., 2000) (Fig. 3). Subsidence was resumed in the Late Permian and,
158 consequently, the South Permian Basin became separated from the North Permian Basin by the
159 Mid North Sea High (Duin et al., 2006). In the study area, Upper Rotliegend terrestrial
160 sandstones of the Slochteren Formation were deposited above the Saalian unconformity to
161 become the major reservoir interval for Permian gas plays (Verweij and Simmelink, 2002) (Fig.
162 3).

163 The Zechstein Sea subsequently flooded the Broad Fourteens Basin in the Late Permian,
164 depositing a thick interval of salt and relatively thin carbonate stringers (van Verweij and
165 Simmelink, 2002; Strozyk et al., 2012) (Unit S2 in Figs. 3, 4 and 5). Zechstein salt caps Upper
166 Rotliegend continental sandstones (Unit S1) and forms an effective seal rock for Permian (and
167 older) strata (Coward, 1995). In the interpreted seismic volume, a high-amplitude seismic

168 reflection separates the Zechstein Group (Unit S2) from Upper Rotliegend reservoirs in Unit
169 S1 (Figs. 4 to 6; Table 1).

170

171 *3.2. Mesozoic*

172 Continental rifting was intensified during the Mesozoic, allowing for differential subsidence to
173 predominate in the Southern North Sea (Alves and Elliott, 2014; Duin et al., 2006) (Fig. 4). In
174 a rapidly subsiding Broad Fourteens Basin, aeolian sands and lacustrine claystones from the
175 Lower and Upper Germanic Trias Group (Unit S3; Fig. 3) were conformably deposited above
176 the Zechstein salt (Van Hulten, 2010). In seismic data, the bright reflection at the base of
177 Germanic Trias Group correlates with a change from the high-velocity Zechstein salt (Unit S2)
178 to the relatively low-velocity aeolian sandstones and lacustrine claystones of the Lower
179 Germanic Trias Group in Unit S3 (Figs. 4 and 5; Table 1). In the study area, the Germanic Trias
180 Group (Unit S3) comprises a package with moderate frequency and moderate- to high-
181 amplitude seismic reflections (Figs. 4 and 6). Aeolian sands and lacustrine claystones of the
182 Lower Germanic Trias Group (Buntsandstein Formation) are a prolific gas reservoir,
183 particularly where Zechstein salt (Unit S2) has been withdrawn and welds have formed
184 between Triassic strata (Unit S3) and the Rotliegend Group in Unit S1 (Van Hulten, 2010).

185 Towards the end of the Triassic, salt tectonics and reactive diapirism became concentrated
186 along extensional boundary faults (Stewart and Coward, 1995; Ziegler, 1992). Rift-raft
187 tectonics led to the further deepening of the Broad Fourteens Basin and the establishment of
188 open marine conditions (Alves and Elliott, 2014; Penge et al., 1993). As a result, the deep-
189 water Altena Shales (Unit S4) were deposited unconformably above the Germanic Trias Group,
190 with the more bituminous Posidonia Shale Formation comprising the source interval for
191 Jurassic oil plays due to a marked segmentation of the Southern North Sea in confined sub-

basins (Duin et al., 2006; Nalpas et al., 1995) (Fig. 3). The Altena Shales (Unit S4) comprise argillaceous deposits, calcareous and clastic sediments (van Verweij and Simmelink, 2002), and form a package of high frequency, continuous and moderate- to high-amplitude reflections in seismic data (Figs. 4 and 6; Table 1).

Deposition of the Altena Shales stopped in the Middle Jurassic during the Mid-Kimmerian upwarping tectonic event (Fig. 3). This upwarping event is a product of salt tectonics, reactive diapirism and thermal upwelling from dolerite intrusions (Van Wees et al., 2000), which occurred in association with the Jurassic Kimmerian tectonic phase (Fig. 3). In areas with the greater uplift, up to 1500 m of Jurassic strata may have been eroded (Heim et al., 2013). Despite this latter uplift event, continuing NE-SW oriented extension compartmentalised the Broad Fourteens Basin, imposing its present-day NW-SE trend (Fig. 1a). Local erosion of Triassic, Zechstein and Rotliegend sequences above active structural highs generated thick successions of the Delfland Subgroup and Vlieland Sandstone, depositing reservoir and seal intervals for oil that was later sourced from the Posidonia Shales (Van Wijhe, 1987; Verweij and Simmelink, 2002; Duin et al., 2006).

The Rijnland Group (Unit S5) comprises coarse clastic intervals, carbonaceous claystones and interbedded sandstones, and was deposited conformably above the Schieland Group (van Verweij and Simmelink, 2002; Van Adrichem Boogaert and Kouwe, 1993) (Fig. 3). Unit S5 is bounded at the top by the Base Tertiary Unconformity (H6), at which level maximum erosion takes place at the crest of a Late Cretaceous anticline (Figs. 4 and 6). In seismic data, Unit S5 forms a package of high-amplitude, high-frequency seismic reflections deformed locally by closely spaced normal faults (Figs. 4 and 6; Table 1).

The Late Cretaceous records a major episode of sea-level rise, accompanied by post-rift subsidence, and led to the accumulation of the Chalk Group (Van Wijhe, 1987; Verweij and

Simmelink, 2002) (Fig. 3). This group (Unit S6) comprises limestones, marls, calcareous claystones and glauconitic sands deposited conformably above the Rijnland Group (van Verweij and Simmelink, 2002) (Figs. 3 and 5). The onset of Alpine compression in the Late Cretaceous interrupted regional subsidence in the Broad Fourteens Basin, with the so called Sub-Hercynian tectonic phase reactivating Variscan faults with a reverse-dextral motion (De Lugt et al., 2003; Nalpas et al., 1995). Maximum erosion of ~ 700 m of strata occurred in the centre of the basin, close to the axis of inversion, herein named Anticline A, affecting the overall thickness of the Chalk Group (Nalpas et al., 1995; De Lugt et al., 2003) (Figs. 4 and 6). Later, the Laramide inversion event in the early Paleocene created a prominent Cretaceous-Tertiary boundary (H6) at the top of Chalk Group (Oudmayer and De Jager, 1993; De Lugt et al., 2003) (Figs. 4 and 6).

3.3. Cenozoic

Cenozoic strata comprise sandstones, clays, silts, locally gravel or peat, and brown coal seams that are part of the North Sea Group, interpreted as Unit S7 in our seismic volume (van Verweij and Simmelink, 2002; Van Adrichem Boogaert and Kouwe, 1993). The North Sea Group directly overlies the Chalk Group (Fig. 5). Where maximum erosion took place around the hinge region of the Late Cretaceous Anticline A, the base of Cenozoic strata directly overlies the Rijnland Group (Unit S5; Figs. 4 and 6). Unit S7 is characterised by a package of high-frequency, continuous and moderate to high-amplitude seismic reflections (Figs. 3 to 5; Table 1).

Three (3) inversion episodes affected the Broad Fourteens Basin in the Cenozoic – the Laramide, Pyrenean and Savian episodes (Fig. 3). The Laramide inversion (early Paleocene) reactivated Sub-Hercynian faults and created a prominent Base Tertiary Unconformity (De

240 Lugt et al., 2003; Oudmayer and De Jager, 1993) (Horizon H6; Figs. 3 to 9). The Pyrenean
241 inversion (Oligocene) created another unconformity at the base of the Miocene strata,
242 separating the Lower from the Middle North Sea Group (Oudmayer and De Jager, 1993; Wong
243 et al., 2001; Verweij and Simmelink, 2002) (Fig. 3). The boundary between the Middle and
244 Upper North Sea Groups (Savian unconformity) marks a break in sedimentation that resulted
245 from regional uplift during the Alpine Orogeny and a global sea-level lowstand (Oudmayer
246 and De Jager, 1993; Wong et al., 2001) (Fig. 3).

247

248 **4. Principal fault geometries**

249 The seismic data show Upper Mesozoic to Paleogene strata offset by deeply rooted listric
250 faults, and deformed by broad anticlines associated with normal faults (Figs. 4 to 6). The TWTT
251 structural maps in Figs. 10 to 12 highlight the main structures interpreted in the study area.

252

253 *4 .1. Listric faults*

254 In the interpreted dataset, listric faults are detached in the Zechstein salt (Unit S2) and
255 accommodated the gravitational gliding of the overburden strata. At the same time, significant
256 subsidence occurred in adjacent hanging-wall blocks (Penge et al., 1999; Alves, 2012; Alves
257 and Elliott, 2014) (Figs. 4, 5 and 8). Variations in thickness between the footwall and the
258 hanging-wall blocks of listric faults reveal that syn-sedimentary growth faults propagated
259 upwards from the Zechstein salt (Unit S2; Figs. 4 to 6).

260 Listric faults offset Units S3, S4 and S5 (Lower and Middle Mesozoic strata), with some
261 propagating vertically into Paleogene strata in Unit S7 (Figs. 5 and 8). They are characterised
262 by a broadly spaced curvilinear pattern in map view, striking in a NW-SE direction that is sub-

263 parallel to the strike of Anticline A (Figs. 10b and 12). Listric faults show trace lengths of 7.2-
264 13.5 km, with a maximum fault throw of 440 m (Figs. 4, 8 and 12).

265

266 *4.2. Tiers of normal faults*

267 Normal faults are closely spaced in Upper Mesozoic and Paleogene strata (Figs. 4 to 6). We
268 grouped these normal faults into two distinct tiers: Tier 1 (Upper Mesozoic) and Tier 2
269 (Paleogene). In the interpreted dataset, periods of fault reactivation below and above the Base
270 Tertiary Unconformity (horizon H6) can be relatively dated. Horizon (H6) forms a high-
271 amplitude, regionally mappable seismic reflector and represents a major change in from the
272 soft Paleogene Lower North Sea clays and silts above (Unit S7) to the harder limestones of the
273 Chalk Group below (Unit S6; Figs. 3 to 5 and 12).

274

275 *4.2.1. Tier 1 faults: Late Mesozoic*

276 Tier 1 faults are closely spaced normal faults formed around the hinge of Anticline A (Figs. 4
277 and 6). These faults predominantly offset Upper Mesozoic strata in Units S5 and S6 (Figs. 4
278 and 6). The upper tips of Tier 1 faults are eroded and truncated by the Base Tertiary
279 Unconformity (horizon H6), with some faults reactivating and extending into Paleogene strata
280 (Figs. 6 to 8). The location of Tier 1 faults around the hinge of Anticline A suggests they are
281 created by outer-arc stretching during buckling and, thus, do not normally accommodate
282 regional extension (see Rowan et al., 1999) (Figs. 4 and 6). Tier 1 faults are grouped into non-
283 reactivated (eroded) and reactivated faults based on their upper tip terminations, as revealed by
284 the seismic sections and throw-depth (T-Z) profiles in Figs. 6, 13 and 14.

285

286 *4.2.1.1. Non-reactivated (eroded) Tier 1 faults*

287 Non-reactivated Tier 1 faults are restricted to the hinge of Anticline A (Figs. 6, 13 and 14).
288 Their upper tip lines are eroded and truncated at the Base Tertiary Unconformity (horizon H6),
289 with no faults propagating upwards into Paleogene strata (Figs. 13 and 14). The relatively large
290 throw values recorded just below horizon H6 confirm the erosion of their upper tips (Figs. 15
291 to 17), suggesting that these faults were active, and offsetting Unit S6, before the erosional
292 event responsible for the Base Tertiary Unconformity (Figs. 3 and 6).

293 Non-reactivated Tier 1 faults are characterised by their closely spaced, linear to curvilinear
294 conjugate pattern and strike predominantly in a NW-SE direction, roughly parallel to the strike
295 of Anticline A (Fig. 10). Thus, their plan-view geometry is controlled by this latter structure
296 (Fig. 10b). Non-reactivated Tier 1 faults show a maximum throw of 34.5 m, a spacing ranging
297 from 560 to 2,300 m, and trace lengths of 1,100-11,250 m (Fig. 10).

298

299 *4.2.1.2. Reactivated Tier 1 faults*

300 Fault reactivation has been described as reflecting the further propagation of pre-existing faults
301 (Holdsworth et al., 1997; Nicol et al., 2005). Tier 1 faults that offset the Base Tertiary
302 Unconformity (horizon H6) and propagate upwards in Paleogene strata are interpreted as
303 reactivated Tier 1 faults (Figs. 6, 13 and 14). Their throws die out upwards into Paleogene
304 strata, contrasting with non-reactivated (eroded) Tier 1 faults that are truncated at level of
305 horizon H6, or just below this latter (Figs. 6, 13 and 14).

306 Reactivated Tier 1 faults are characterised by their linear to curvilinear pattern, and were
307 predominantly reactivated above Anticline A in the southern part of the study area (Fig. 12).
308 The faults have a maximum throw of 40.2 m, a spacing of 840-5,200 m, and trace lengths of

1,200-12,250 m (Fig. 12). Some reactivated Tier 1 faults intersect the relatively deep listric faults, thus potentially forming secondary migratory pathways for hydrocarbons into shallower Paleogene units (Figs. 6, 8 and 14).

4.2.1. Tier 2 faults: Paleogene

Tier 2 faults comprise densely spaced sets of normal faults with a discrete range of strikes, and reveal an irregular polygonal geometry in map view (Figs. 5, 6, 9 and 11). The upper and lower tip lines of these faults die out in Paleogene strata, with some faults propagating downward and offsetting the Base Tertiary Unconformity (horizon H6) around the hinges of Anticlines B and C, a character particularly observed towards the northern part of the study area (Fig. 12). These faults initially formed as polygonal faults and were reactivated to form new fault segments, or lengthen their sizes, due to later tectonic deformation (Figs. 5, 9 and 11).

Tier 2 faults have a maximum throw of 9.8 m, a spacing of 320-680 m, and trace lengths of 950-2,000 m. They also accommodate a significant part of the local stretching affecting the Paleogene overburden (Figs. 9 and 11). The geometry of Tier 2 faults likely resulted from near-seafloor extension over growing anticlines, which affected compacting mud-rich strata (Lonergan et al., 1998; Cartwright et al., 2003).

5. Effect of lithology on fault throw distribution

The interpreted faults F1 to F6 are characterised by their maximum throw of 32 ms (40.2 m), an average spacing of 560 m, and trace lengths ranging from 1,100-11,250 m. These faults offset a layered succession comprising sands and shales (Figs. 15 to 20). Importantly,

differences in fault throw are observed when the fault strands in the sand-rich intervals are compared to fault segments in the shale-rich intervals. In the sand-rich intervals, fault throws are larger (average 32 ms, or 40.3 m) compared to the smaller fault throws (average 13.5 ms, or 17.7 m) documented in the shale rich-intervals (Figs. 15-20).

A decrease in fault throw is observed as the faults propagate from sand-rich into shale-rich intervals (Figs. 15 to 20). Hence, the propagation of fault segments, first grown in sand-rich strata, into shale intervals can result in vertically segmented fault arrays, as revealed by the throw-depth (T-Z) data in Figs. 15 to 20. Nevertheless, further propagation of two hard-linked fault segments after their growth can attenuate the throw variations recorded on T-Z profiles, and thus obscure differences in the throw distribution with depth.

6. Propagation and growth history of faults

6.1. Fault nucleation

The relative nucleation of representative faults F1 to F6 in the study area is illustrated with reference to the throw-depth (T-Z) profiles in Figs. 15 to 20. Fault segments with throws between 16 ms and 32 ms (20.2 m and 40.3 m) are early-stage fault segments and represent regions where faults nucleated first in competent sand and limestone intervals (Figs. 15 to 20). Each segment of these early-stage faults propagated outwards until they encountered other fault strands to link with. Linkage points are recorded in less competent shale-rich intervals where throw minima vary between 2 ms and 14 ms (2.5 m to 17.7 m) (Figs. 15 to 20) (Ellis and Dunlap, 1988; Mansfield and Cartwright, 1996). Hence, we interpret regions with local throw maxima in the throw-depth (T-Z) profiles as the first loci of fault growth, which dominantly occurred in competent sand and limestone intervals (Figs. 15b to 20b).

354

355 *6.2. Modes of fault growth*

356 We recognise two (2) distinct modes of fault growth, as revealed by the throw-depth profiles
357 in Figs. 15 to 22. These modes include fault growth via upward propagation and segment
358 linkage. Listric faults that reflect the early-stage deformation of Mesozoic strata grew via the
359 upward propagation from a parent fault above the Zechstein salt (Unit S2; Figs. 4 to 6). These
360 faults exhibit a typical vertical, positive stepped throw gradient (Fault F7; Fig. 21). They show
361 major breaks in throw gradients around the top of Jurassic strata. The fault strands below the
362 top Jurassic marker (horizon H4a) offset Triassic-Jurassic strata and show throw maxima
363 between 42 ms and 85 ms (52.9 m to 129 m) (Fig. 21). The strands above the top Jurassic
364 marker offset Cretaceous strata and reveal abrupt steps in throw profiles, with throws reaching
365 values between 15 ms and 32 ms (18.9 m to 40.3 m) (Fig. 21).

366 The upward decrease in throw values, and the vertical positive step in throw gradients recorded
367 by listric fault F7, are related to fault growth by upward propagation from parent faults above
368 the Zechstein salt (Unit S2; Figs. 4 to 6). The absence of alternating local throw maxima and
369 minima on the throw distribution profiles reflects the growth of listric faults by upward
370 propagation (Fig. 21). Also, thickness variations between the footwall and the hanging-wall
371 blocks of listric faults show these are syn-sedimentary faults that propagated vertically during
372 their growth (Figs. 4 to 6).

373 The representative vertical throw-depth (T-Z) profiles in Figs. 15b to 20b and 22c show a
374 distinct mode of growth dominated by segment linkage. This mode of fault growth is
375 recognised by its stepped vertical throw-depth (T-Z) profiles with breaks in throw gradients
376 (Figs. 15b to 20b and 22c). Sharp changes in throw values are interpreted to be a consequence
377 of reactivation and growth by segment linkage, where two separate faults have propagated

towards each other. Segments with local throw maxima are early-stage fault-segments formed in regions where faults nucleated first in more competent (sand-rich) intervals. Each fault segment is separated by a local throw minimum in less competent (shale-rich) intervals, as expected for this type of growth by segment linkage (Figs. 15b to 20b and 22c).

Abrupt changes in fault throw are interpreted as a characteristic of fault reactivation and can be attributed to lithological effects during fault propagation through mechanical barriers (Figs. 15b to 20b). Contrasts in acoustic impedance of the sediments along the fault planes are sufficient to infer such major change in throw gradients. Fault growth via segment linkage has wider implications for reactivation processes in fault systems, particularly where more competent (strong) mechanical layers favour the nucleation of new faults in distinct mechanical intervals (Peacock and Sanderson, 1992; Childs et al., 1996) (Figs. 15 to 20).

7. Discussion

7.1. Impact of tectonic shortening on the geometry and reactivation of supra-salt faults

Fault reactivation has been described as reflecting the further propagation of pre-existing faults after a significant period of inactivity (Holdsworth et al., 1997; Nicol et al., 2005). The ability for a fault to repeatedly reactivate is directly related to the orientation of the fault planes with respect to the principal stresses (White et al., 1986; Richard and Krantz, 1991), and the mechanical properties of the fault surface or zone itself: a) fault cohesion, faults' coefficient of friction on the fault surface, and c) fluid pressure controlled by regional tectonics (Ward et al., 2016; Ferrill et al., 2017).

The Late Cretaceous to Paleogene tectonic inversion episodes (i.e. Sub-Hercynian, Laramide, Pyrenean and Savian episodes; Figs. 3 and 23), have induced a continuum of deformation in

401 the Broad Fourteen Basin, Southern North Sea, and contributed significantly to the formation
402 and subsequent reactivation of Upper Mesozoic to Paleogene supra-salt faults (Figs. 4, 5 and
403 23). In the study are, we recognise two distinct tiers of faults according to their geometry: a)
404 Tier 1 faults (Upper Mesozoic), and b) Tier 2 faults (Paleogene) (Figs. 4 to 6). Tier 1 faults
405 resulted from the progressive buckling and stretching of outer arc Mesozoic strata during the
406 Late Cretaceous inversion episode, i.e. during Sub-Hercynian tectonics (Figs. 3, 4 and 24c,d).

407 The Laramide inversion episode (Early Paleocene) reactivated Sub-Hercynian Tier 1 faults and
408 created a prominent Late Cretaceous-Tertiary unconformity (horizon H6) (De Lugt et al., 2003;
409 Oudmayer and De Jager, 1993). This same horizon H6 is a strong, regionally mappable seismic
410 reflector and represents a major change in rock strength from softer Tertiary clays and silts of
411 the North Sea Group (Unit S7) to stiffer Upper Cretaceous limestones deposits of the Chalk
412 Group below (Unit S6; Figs. 3, 4, 23 and 24e). The upper tip lines for these Tier 1 faults were
413 eroded by the Paleocene Laramide erosional event at the Base Tertiary Unconformity (H6;
414 Figs. 13 and 14), suggesting they were actively offsetting Upper Mesozoic strata before the
415 start of the Laramide erosional event (Fig. 24c and d). Subsequently, the Pyrenean (Oligocene)
416 and Savian (Miocene) inversion episodes reactivated some of these faults upwards into
417 Paleogene strata (Unit S7), where they link with the overlying Tier 2 faults (Figs. 6, 23 and
418 24e).

419 The TWTT structural maps in Fig. 12 highlight the map view of these fault tiers. Tier 1 faults
420 were largely reactivated around the hinge of Late Mesozoic Anticline A, whereas the overlying
421 Tier 2 faults were selectively reactivated around the hinges of Anticline B and C (Fig. 12). This
422 observation suggests that in addition to the fault's orientation and geometry (Richard and
423 Krantz, 1991; Baudon and Cartwright, 2000) other controls, such as the location of the

underlying anticlines, affected fault reactivation in the study area, as observed on the TWTT map in Fig. 12.

The distinct geometries observed in Tier 1 and 2 faults can be attributed to the mechanical differences in different lithological intervals and deformation mechanisms (Figs. 10 and 11). The tectonic shortening and brittle deformation experienced by the more competent carbonate and sand-rich strata of the Chalk and Rijnland Groups led to more localised linear-curvilinear geometries in Tier 1 faults (Fig. 10), whereas compactional loading (diagenesis) and the relatively ductile deformation of the incompetent mud-rich strata of the Lower North Sea Group resulted in diffuse strain and the generation of a polygonal pattern in Tier 2 faults (Figs. 11). The polygonal pattern in Tier 2 faults was likely formed from near-seafloor extensional stresses predominating over growing anticlines, accompanied by the sudden compaction of mud-rich strata and subsequent loss of volume and fluid (Lonergan et al., 1998; Cartwright et al., 2003) (Fig. 11). Nevertheless, some of the Tier 2 faults still record the effect of Miocene inversion episode (Savian phase) which largely reactivated and lengthen some of these latter faults downwards around the hinge of Anticlines B and C (Figs. 5, 9 and 12).

According to the analogue sandbox experiments presented in Gabrielsen et al. (2016) incompetent layers, or intervals, with a ductile behaviour can prevent fault propagation or lead to vertical segmentation (decoupling) when fault segments are subjected to various types of linkage across ductile layers. In the study area, we observe vertical fault segmentation in both seismic and throw-depth (T-Z) profiles (Figs. 9, 15b, 16b, 17b and 22c). Several fault segments with relatively small throws are observed in shale-rich intervals, while faults in the sand-rich intervals appear as discrete, isolated faults recording the largest throws (Figs. 15b, 16b, 17b, 19c and 22c).

447 The effect of incompetent layers on the segmentation of faults has been studied at outcrop and
448 using seismic data (Soliva et al. 2005; Schöpfer et al. 2006; Libak et al., 2019; Ferrill et al.
449 2017). For instance, Libak et al. (2019) recently interpreted seismic data from the Norwegian
450 Barents Sea to show that fault zones are more segmented and wider in claystones, while faults
451 in sandy intervals are narrower and more localised, thus less segmented. Deformation tends to
452 be more localised (less segmented) to reveal local throw maxima in competent lithologies such
453 as sandstones and carbonates, and more distributed (segmented) in incompetent lithologies
454 such as claystones and shales, where throw minima are recorded (Schöpfer et al. 2006).

455 Research has also shown that faults are often steep in competent lithologies, while faults have
456 more gentle dips in relatively incompetent strata (Peacock 2002; Ferrill et al. 2017). Such
457 differences in fault dip along a fault segment can locally lead to fault refraction, which may
458 generate extensional (dilatational) jogs (Peacock and Sanderson 1991; Ferrill et al. 2017). In
459 the study area, no evidence exists for changes in fault dip geometries, as faults propagate from
460 competent into incompetent intervals. This is often due to intricate fault geometries of a
461 particular area or, instead, a result of the limited resolution of seismic datasets, i.e. the faults
462 are not fully resolved by the seismic data. In the study area, the lack of variation in fault dips
463 is interpreted as reflecting the deformation of the original dip-linkage structures during post-
464 linkage slip of the faults, with any original topological irregularities having been largely
465 eliminated during fault reactivation.

466

467 *7.2. Propagation and growth history of faults in layered successions*

468 Interpreted faults F1 to F6 and F8 to F11 reveal a break in throw gradients, and a progressive
469 decrease in throw towards the fault tips, a characteristic of reactivation and growth during fault
470 propagation through mechanical barriers (Gross et al., 1997; Wilkins and Gross, 2002) (Figs.

15b to 20b and 22c). Research has shown that, as strain accumulates in a layered sedimentary sequence, competent (brittle) lithologies such as limestones and sandstones accommodate smaller amounts of pre-failure strain and are able to fracture first, whereas incompetent (ductile) lithologies such as claystones and shales accommodate higher prefailure strain prior to faulting and usually fracture later (Ferrill and Morris, 2003, 2008; Welch et al., 2009). Hence, faults would be expected to nucleate first in competent lithologies with the larger throws, and this study show this to be the case (Figs. 15 to 20).

The results in this work show differences between the throw magnitudes of faults in sand-rich intervals (with a throw maximum of 32 ms, or 40.3 m) compared to the shale-rich intervals (with a throw maximum of 14 ms, or 17.7 m) (Figs. 15 to 20). This difference can be related to the predominance of brittle deformation in the competent sand-rich intervals, resulting in a less segmented zones of fault deformation with local throw maxima, while ductile deformation in incompetent shale-rich interval led to a more segmented zone of deformation, with local throw minima (Figs. 15b to 20b and 22c). Thus, fault segments with local throw maxima in the throw-depth (T-Z) profiles are interpreted to be the loci where faults nucleated first, with this occurring predominantly in competent sand-rich intervals (Figs. 15 to 20). These fault segments drove displacement into shale-rich intervals where smaller fault throws are accommodated by more ductile deformation (Figs. 15 to 20).

In our throw-depth (T-Z) profiles there is evidence for vertical fault segmentation, where the fault segments with local throw minima in the shale-rich intervals were linked to pre-existing fault segments with local throw maxima in the sand-rich intervals (Figs. 15b to 20b). Thus, the propagation of slip from fault segments with local throw maxima (in the sand-rich intervals) into the shale-rich intervals can describe the vertically segmented fault arrays observed in the throw-depth (T-Z) profiles in Figs. 15b to 20b and 22c. The results of our throw-depth (T-Z) interpretation support the view that vertically segmented fault arrays initially nucleated in the

competent, and brittle, lithologies (sandstones and limestones) with less segmented maximum throws, and were later linked by faults in the incompetent, ductile, lithologies (shales) with more segmented, minimum throws (Peacock and Sanderson, 1992; Childs et al., 1996) (Figs. 15b to 20b).

Differences in the throw distribution provide insights into the recognition of two (2) distinct modes of fault growth: fault growth via upward propagation vs. fault segment linkage. The listric fault F7 (Fig. 21) shows a regular upward decrease in throw values and maintains vertical, positively stepped gradients, revealing the classical model for fault growth by upward propagation from pre-existing faults above thick salt (Richard and Krantz, 1991; Baudon and Cartwright, 2008; Maunde and Alves, 2020) (Fig. 21). The maximum throw value on the throw profile marks the onset of faulting; thus, faulting started above the Permian Zechstein salt (Figs. 6 and 21).

The interpreted faults F1 to F6 and F8 to F11 present throw-depth (T-Z) profiles with multiple local throw maxima separated by local throw minima, revealing fault growth via segment linkage (Baudon and Cartwright, 2008; Kim and Sanderson, 2005) (Figs. 15b to 20b and 22c). Fault segments with local throw maxima represent the intervals where faults nucleate first in more competent sand-rich intervals. Each of these fault segments propagated outwards until they encountered other pre-existing fault segments to link with. The zone of linkage between two originally individual segments that are linked is recognisable by a zone of local throw minima and steepening of the throw gradients (Cartwright et al., 1995; Lohr et al., 2008). (Figs. 15b to 20b). However, further propagation of the two hard-linked fault segments after growth might attenuate the throw variations and obscure differences in the throw distribution (Figs. 18b and 20b).

519 The interpreted fault tiers are largely segmented and may present an important limitation for
520 the implementation of carbon capture and storage (CCS) in the Broad Fourteens Basin (Figs.
521 15b to 20b and 22c). For example, the locus of fault segment linkage may increase the
522 permeability of the rocks. Where the fault segments interact, active fracturing provides a
523 pathway for fluids, as well as increasing the chances of compartmentalisation or localised fluid
524 flow through the fault linkages (Curewitz and Karson, 1997; Ward et al., 2016), thus revealing
525 significant risks when injecting CO_2 into the subsurface. In the Broad Fourteens Basin, listric
526 faults control and transmit fluids within, and between Mesozoic strata (Penge et al., 1999;
527 Alves and Elliott, 2014). The reactivated Tier 1 faults intersecting these deeply rooted listric
528 faults potentially allow secondary migration of hydrocarbons into shallower Paleogene
529 reservoirs (Figs. 8 and 24e).

530 The models for the evolution of interpreted faults in Fig. 24 provide insights into the timing of
531 fault activity, with a direct application to hydrocarbon migration and sealing of faults in
532 petroleum reservoirs. For instance, the relative timing of any fault reactivation phases with
533 reference to the filling of hydrocarbon traps would be critical for an evaluation of seal risk
534 (Cartwright et al., 2007). A further understanding of reactivation processes will greatly improve
535 petroleum prediction of seal integrity, trap geometry and fluid migration into shallow reservoirs
536 in the Broad Fourteens Basin, Southern North Sea.

537

538 **8. Conclusions**

539 Detailed mapping and geometric analyses of normal faults using high-quality 3D seismic and
540 borehole data from the Broad Fourteens Basin, offshore The Netherlands, provided important
541 insights into the geometry and reactivation histories of Upper Mesozoic to Paleogene supra-
542 salt faults. The key conclusions of this study are as follows:

1. In the Broad Fourteen Basin, Southern North Sea, the Late Cretaceous to Paleogene tectonic inversion episodes induced a continuum of internal deformation and contributed significantly to the formation and subsequent reactivation of supra-salt faults. Such a phenomenon had a positive economic impact, as reactivated faults potentially allowed the secondary migration of hydrocarbons into shallower reservoir units.
2. Two distinct tiers of fault geometry are recognised in the study area: a) Tier 1 faults (Late Mesozoic) resulting from local buckling and stretching of outer arc Mesozoic strata during the Late Cretaceous-Paleogene tectonic inversion episodes (i.e. Sub-Hercynian, Laramide, Pyrenean and Savian phases), b) Tier 2 faults (Paleogene) relating to early diagenesis but still recording the effect of a Paleogene inversion episode. All in all, the geometry and location of underlying anticlinal structures affected the selection of reactivation and growth histories of the interpreted fault tiers.
3. The truncation and lack of near-zero throw values at the Base Tertiary Unconformity, revealed by Tier 1 faults, confirm the erosion of the upper fault tips by a Paleocene-Laramide erosional event. This truncation suggests that Tier 1 faults were active in the Upper Cretaceous Chalk Group before the onset of a Paleocene erosional event in the Southern North Sea.
4. Notable differences in fault throw values are observed between sand- and shale-rich intervals. In sand-rich intervals, fault throws are larger (32 ms or 40.3 m) compared to shale-rich intervals (14 ms or 17.7 m). Hence, families of vertically segmented fault arrays are observed in the throw-depth profiles, as faults propagated through alternating sand-shale intervals.
5. The interpreted fault tiers are segmented, increasing the chances of compartmentalisation, or localised fluid flow, through fault linkage points. In the Broad Fourteens Basin, listric

faults provide significant pathways for fluid migrating from pre-Zechstein salt units into Mesozoic strata. Consequently, Tier 1 faults intersecting these deeply rooted listric faults will potentially allow the secondary migration of hydrocarbons into shallower reservoir units.

Acknowledgements

Petroleum Technology Development Fund (PTDF), Nigeria (Ref: PTDF/ ED/PHD/MA/1328/18) was greatly acknowledged and thanked for funding the research study. We acknowledge the permission conceded by Haloil for the use of the data included in this paper and Schlumberger for the provision of Petrel® software for seismic interpretation.

References

Alves, T.M., 2012. Scale-relationships and geometry of normal faults reactivated during gravitational gliding of Albian rafts (Espírito Santo Basin, SE Brazil). Earth Planet. Sci. Lett. 331, 80–96.

Alves, T. M. and Elliott, C. 2014. Fluid flow during early compartmentalisation of rafts: A North Sea analogue for divergent continental margins. Tectonophysics, 634**,** 91-96.

Baudon, C., Cartwright, J., 2008. The kinematics of reactivation of normal faults using high resolution throw mapping. J. Struct. Geol. 30, 1072–1084.

Bahroudi, A., Koyi, H.A., Talbot, C.J. 2003. Effect of ductile and frictional décollements on style of extension. Journal of Structural Geology, 25, 1401–1423.

589 Bentham, M., Green, A., Gammer, D., 2013. The occurrence of faults in the Bunter Sandstone
590 Formation of the UK sector of the Southern North Sea and the potential impact on storage
591 capacity. Energy Procedia 37, 5101–5109.

592 Brown, A.R., 2003. Interpretation of Three-dimensional Seismic Data, sixth ed., vol. 42.
593 American Association of Petroleum Geologists Memoir, p. 541

594 Caine, J.S., Evans, J.P., Forster, C.B., 1996. Fault zone architecture and permeability structure.
595 Geology, 24, 1025–1028.

596 Cartwright, J., James, D., Bolton, Al, 2003. The genesis of polygonal fault system: a review.
597 Geol. Soc. Lond. Spec. Publ. 216, 223–243.

598 Cartwright, J.A., Trudgill, B.D., Mansfield, C.S., 1995. Fault growth by segment linkage: an
599 explanation for scatter in maximum displacement and trace length data from the
600 Canyonlands Grabens of SE Utah. Journal of Structural Geology 17 (9), 1319–1326.

601 Cartwright, J., Huuse, M., Aplin, A., 2007. Seal bypass systems. American Association of
602 Petroleum Geologists Bulletin 91 (8), 1141–1166.

603 Cartwright, J.A., Mansfield, C.S., 1998. Lateral displacement variation and lateral tip geometry
604 of normal faults in the Canyonlands National Park, Utah. J. Struct. Geol. 20, 3–19.

605 Childs, C., Nicol, A., Walsh, J.J., Watterson, J., 1996. Growth of vertically segmented normal
606 faults. J. Struct. Geol. 18, 1389-1397.

607 Coward, M., 1995. Structural and tectonic setting of the Permo-Triassic basins of northwest
608 Europe. Geological Society, London, Special Publications, 91**,** 7-39.

609 Curewitz, D., Karson, J.A., 1997. Structural settings of hydrothermal outflow: fracture
610 permeability maintained by fault propagation and interaction. J. Volcanol. Geotherm.
611 Res. 79, 149–168.

De Lugt, I. R., Van Wees, J. D. and Wong, T. E. 2003. The tectonic evolution of the southern Dutch North Sea during the Palaeogene: basin inversion in distinct pulses. Tectonophysics, 373**,** 141-159.

Duin, E., Doornenbal, J., Rijkers, R., Verbeek, J. and Wong, T. E. 2006. Subsurface structure of the Netherlands-results of recent onshore and offshore mapping. Netherlands Journal of Geosciences, 85**,** 245.

Ferrill, D.A., Morris, A.P., 2003. Dilational normal faults. J. Struct. Geol. 25, 183-196.

Ferrill, D.A., Morris, A.P., 2008. Fault zone deformation controlled by carbonate mechanical stratigraphy, Balcones fault system, Texas. AAPG Bull. 92, 359-380.

Ferrill, D.A., McGinnis, R.N., Morris, A.P., McGinnis, R.N., Smart, K.J., Wigginton, S. S., Hill, N.J., 2017. Mechanical stratigraphy and normal faulting. Review article. J. Struct. Geol. 94, 275-302.

Ferrill, D.A., Morris, A.P., McGinnis, R.N., 2012. Extensional fault-propagation folding in mechanically layered rocks: the case against the frictional drag mechanism. Tectonophysics 576-577, 78-85.

Faulkner, D.R., Jackson, C.A.L., Lunn, R.J., Schlische, R.W., Shipton, Z.K., Wibberley, C. A.J., Withjack, M.O., 2010. A review of recent developments concerning the structure, mechanics, and fluid flow properties of fault zones. J. Struct. Geol. 32, 1557–1575.

Ellis, M. A., Dunlap, W. J. 1988. Displacement variation along thrust faults: Implications for the development of large faults. Journal of Structural Geology, 10, 183- 192

Gartrell, A., Lils, M., Underschultz, J., 2002. Controls on the trap integrity of the Skua oil field, Timor Sea. In: Keep, M., Moss, S.J. (Eds.), The Sedimentary Basins of Western Australia 3: Proceedings of the Petroleum Exploration Society of Australia Symposium,

635 pp. 389–407. Perth

636 Gabrielsen, R.H., Sokoutis, D., Willingshofer, E., Faleide, J.I. 2016. Fault linkage across weak
637 layers during extension: an experimental approach with reference to the Hoop Fault
638 Complex of the SW Barents Sea. Petroleum Geoscience, 22, 123–135.

639 Gerling, P., Geluk, M., Kockel, F., Lokhorst, A., Lott, G. and Nicholson, R. 1999. 'NW
640 European Gas Atlas'–new implications for the Carboniferous gas plays in the western
641 part of the Southern Permian Basin. Geological Society, London, Petroleum Geology
642 Conference series, 1999. Geological Society of London, 799-808.

643 Gross, M.R., Gutiérrez-Alonso, G., Bai, T., Wacker, M.A., Collinsworth, K.B. 1997. Influence
644 of mechanical stratigraphy and kinematics on fault scaling relations. Journal of Structural
645 Geology, 19, 171–183, https://doi.org/10.1016/S0191-8141 (96)00085-5

646 Hardman, R., Booth, J., 1991. The significance of normal faults in the exploration and
647 production of North Sea hydrocarbons. Geol. Soc. Lond., Spec. Publ. 56, 1–13

648 Heim, S., Lutz, R., Nelskamp, S., Verweij, H., Kaufmann, D., Reinhardt, L., 2013. Geological
649 evolution of the North Sea: cross-border basin modeling study on the Schillground High.
650 Energy Procedia 40, 222–231.

651 Holdsworth, R.E., Butler, C.A., Roberts, A.M., 1997. The recognition of reactivation during
652 continental deformation. Journal of the Geological Society London 154, 73–78.

653 Hooper, E.C.D., 1991. Fluid migration along growth faults in compacting sediments. Journal
654 of Petroleum Geology 14 (2), 161–180.

655 Isaksen, G. H., 2004. Central North Sea hydrocarbon systems: Generation, migration,
656 entrapment, and thermal degradation of oil and gas. AAPG bulletin, 88**,** 1545-1572.

Knai, T.A., Knipe, R.J. 1998. The Impact of Faults on Fluid Flow in the Heidrun Field. In: Jones, G., Fisher, Q.J. & Knipe, R.J. (eds) Faulting, Fault Sealing and Fluid Flow in Hydrocarbon Reservoirs. Geological Society, London, Special Publications, 147, 269–282, https:// doi.org/10.1144/GSL.SP.1998.147.01.18

Laubach, S.E., Olson, J.E., Gross, M.R., 2009. Mechanical stratigraphy and fracture stratigraphy. AAPG Bull. 93, 1413-1426.

Libak, A., Torabi, A., Alae, B., 2019. Normal fault geometric attribute variations with lithology: examples from the Norwegian Barents Sea. Geol. Soc. Lond. Spec. Publ. 495 https://doi.org/10.1144/SP495-2018-164.

Lohr, T., Krawczyk, C.M., Oncken, O., Tanner, D.C., 2008. Evolution of a fault surface from 3D attribute analysis and displacement measurements. J. Struct. Geol. 30, 690–700.

Lonergan, L., Cartwright, J.A., Jolly, R., 1998. 3-D geometry of polygonal fault systems. J. Struct. Geol. 20, 529–548.

Mansfield, C.S., Cartwright, J., 2001. Fault growth by linkage: observations and implications from analogue models. J. Struct. Geol. 23, 745–763.

Mansfield, C.S., Cartwright, J.A., 1996. High resolution fault displacement mapping from three-dimensional seismic data: evidence for dip linkage during fault growth. J. Struct. Geol. 18, 249-263.

Maunde. A., Alves. T.M., Moore. G.F., 2021. Shallow fault systems of thrust anticlines responding to changes in accretionary prism lithology (Nankai, SE Japan). Tectonophysics 812 (2021) 228888, https://doi.org/10.1016/j.tecto.2021.228888.

Maunde. A., and Alves, T.M., 2020. Impact of tectonic rafts' gravitational instability on fault reactivation and geometry. J. Struct. Geol. 130, 103916.

680 Nalpas, T., Le Douaran, S., Brun, J.P., Unternehr, P., Richert, J.P., 1995. Inversion of the Broad
681 Fourteens Basin (offshore Netherlands), a small-scale model investigation. Sedimentary
682 Geology, 95**,** 237-250.

683 Nicol, A., Walsh, J., Berryman, K., Nodder, S., 2005. Growth of a normal fault by the
684 accumulation of slip over millions of years. Journal of Structural Geology 27 (2), 327–
685 342.

686 Oudmayer, B. C. and De Jager, J. 1993. Fault reactivation and oblique-slip in the Southern
687 North Sea. In: Parker, J. R., ed. Petroleum Geology of Northwest Europe: Proceedings
688 of the 4th Conference, 1993 London. The Geological Society, 1281-1290.

689 Peacock, D.C.P., Sanderson, D.J., 1992. Effects of layering and anisotropy on fault geometry.
690 J. Geol. Soc. Lond. 149, 793-802.

691 Peacock, D.C.P., Sanderson, D.J., 1991. Displacements, segment linkage and relay ramps in
692 Normal fault zones. J. Struct. Geol. 13, 721–733.

693 Penge, J.,Munns, J.W., Taylor, B., Windle, T.M.F., 1999. Rift-raft tectonics: examples of
694 gravitational tectonics from the Zechstein basins on northwest Europe. In: Fleet, A.J.,
695 Boldy, S.A.R. (Eds.), Petroleum Geology of Northwest Europe, Proceedings of the 5th
696 Conference, pp. 201–213.

697 Richardson, N.J., Underhill, J.R., Lewis, G., 2005. The role of evaporite mobility in modifying
698 subsidence patterns during normal fault growth and linkage, Halten Terrace, Mid-
699 Norway. Basin Research, 17, 203–223.

700 Richard, P., Krantz, R.W., 1991. Experiments on fault reactivation in strike-slip mode.
701 Tectonophysics 188 (1-2), 117–131.

Rowan, M. G., Jackson, M. P. A., Trudgill, B. D. 1999. Salt-related fault families and fault welds in the northern Gulf of Mexico. AAPG Bulletin, 83, 1454-1484.

Schöpfer, M.P.J., Childs, C., Walsh, J.J., 2006. Localization of normal faults in multilayer sequences. Journal of Structural Geology, 28, 816–833, https://doi.org/10.1016/j.jsg.2006.02.003.

Soliva, R., Schultz, R.A., Benedicto, A., 2005. Three-dimensional displacement-length scaling and maximum dimension of normal faults in layered rocks. Geophysical Research Letters, 32, 1–4, https://doi.org/10. 1029/2005GL023007

Strozyk. F., van Gent. H.W., Urai. J., Kukla. P.A., 2012. 3D seismic study of complex intra-salt deformation: An example from the Upper Permian Zechstein 3 stringer, western Dutch Offshore. Geological Society London Special Publications 363(1):489-501, DOI: 10.1144/SP363.23

Stewart, S.A., Coward, M.P., 1995. Synthesis of salt tectonics in the southern North Sea, UK. Marine and Petroleum Geology, 12, 457–475.

Tao, Z, Alves, T.M., 2019. Impacts of data sampling on the interpretation of normal fault propagation and segment linkage. Tectonophysics, 762, 79-96.

Van Balen, R., Van Bergen, F., De Leeuw, C., Pagnier, H., Simmelink, H., Van Wees, J. and Verweij, J. 2000. Modelling the hydrocarbon generation and migration in the West Netherlands Basin, the Netherlands. Geologie en Mijnbouw, 79**,** 29-44.

Van Hulten, F. F. N. 2010. Geological factors effecting compartmentalization of Rotliegend gas fields in the Netherlands. Geological Society, London, Special Publications, 347**,** 301-315.

724 Van Adrichem Boogaert, H. and Kouwe, W. 1993. Stratigraphic nomenclature of the
725 Netherlands, revision, and update by RGD and NOGEPA. Mededelingen Rijks
726 Geologische Dienst, 50**,** 1-40.

727 Van Wijhe, D. V. 1987. Structural evolution of inverted basins in the Dutch offshore.
728 Tectonophysics, 137**,** 171-219.

729 Van Verweij, J. M. and Simmelink, H. J. 2002. Geodynamic and hydrodynamic evolution of
730 the Broad Fourteens Basin (The Netherlands) in relation to its petroleum systems. Marine
731 and Petroleum Geology, 19**,** 339-359.

732 Van Wees, J.-D., Stephenson, R., Ziegler, P., Bayer, U., McCann, T., Dadlez, R., Gaupp, R.,
733 Narkiewicz, M., Bitzer, F., Scheck, M., 2000. On the origin of the southern Permian
734 Basin, central Europe. Mar. Pet. Geol. 17, 43–59.

735 Ward, N.I., Alves, T.M., Blenkinsop, T.G., 2016. Reservoir leakage along concentric faults in
736 the Southern North Sea: Implications for the deployment of CCS and EOR techniques.
737 Tectonophysics 690, 97-116

738 Welch, M.J., Davies, R.K., Knipe, R.J., Tueckmantel, C., 2009. A dynamic model for fault
739 nucleation and propagation in a mechanically layered section. Tectonophysics 474, 473-
740 492.

741 White, S.H., Bretan, P.G., Rutter, E.H., 1986. Fault-zone reactivation: kinematics and
742 mechanisms. Philosophical Transactions of the Royal Society of London A317, 81–97.

743 Withjack, M.O., Callaway, S., 2000. Active normal faulting beneath a salt layer: An
744 experimental study of deformation patterns in the cover sequence. AAPG Bulletin, 84,
745 627–651.

746 Wilkins, S.J., Gross, M.R., 2002. Normal fault growth in layered rocks at Split Mountain, Utah:
747 influence of mechanical stratigraphy on dip linkage, fault restriction and fault scaling.
748 Journal of Structural Geology 24 (9), 1413–1429.

749 Wiprut, D., Zoback, M.D., 2000. Fault reactivation and fluid flow along a previously dormant
750 normal fault in the northern North Sea. Geology 28, 595–598.

751 Wiprut, D., Zoback, M.D., 2002. Fault reactivation, leakage potential, and hydrocarbon column
752 heights in the northern North Sea. Norwegian Petroleum Society Special Publications
753 Vol. 11, pp. 203–219.

754 Wong, T. E., Parker, N. & Horst, P. 2001. Tertiary sedimentary development of the Broad
755 Fourteens area, the Netherlands. Geologie en Mijnbouw, 80**,** 85-94.

756 Ziegler, P. A. 1990. Geological atlas of western and central Europe, Shell Internationale
757 Petroleum, Maatschappij B.V., The Hague.

758

759

760 **Figure captions**

761 **Fig. 1.** a) Map of the Southern North Sea highlighting its Dutch offshore sector and the location
762 of the study area in the northern end of the Broad Fourteens Basin (BFB), offshore The
763 Netherlands, b) TWTT structural map of the Base Tertiary Unconformity (H6) showing the
764 location of exploration wells and key seismic lines.

765 **Fig. 2.** Schematic cross-section showing the points of fault throw-depth (T-Z) measurements
766 (a) and corresponding throw-depth (T-Z) plot (b). Local throw maxima in the throw-depth plot
767 represent the interval where fault nucleated first..

768 **Fig. 3.** Simplified seismic-stratigraphic correlation between interpreted seismic units and the
769 formal stratigraphic units recognised in the Dutch Sector of the Southern North Sea. Main
770 stratigraphic groups, tectonic phases and unconformities related to regional tectonic events are
771 based on Penge et al. (1999) and van Verweij and Simmelink (2002). Horizons H1-H6, and
772 Units S1-S7 refer to interpreted seismic horizons and units, respectively. The location of the
773 seismic line is shown in Figs. 1b, 10, 11 and 12.

774 **Fig. 4.** a) Uninterpreted and b) interpreted seismic profiles revealing the distinct geometry of
775 Upper Mesozoic (Tier 1) and Paleogene (Tier 2) faults formed over Anticline A. These fault
776 tiers are separated by the Base Tertiary Unconformity (horizons H6). Tier 1 faults responded
777 to Late Cretaceous to Paleogene tectonic inversion episodes, whereas Tier 2 faults resulted
778 from: i) near-seafloor extension over growing anticlines, and ii) sudden compaction of mud-
779 rich strata with subsequent loss of volume and fluid, forming polygonal fault geometries. The
780 location of the seismic line is shown in Figs. 1b, 10, 11 and 12.

781 **Fig. 5.** a) Uninterpreted and b) interpreted seismic profiles showing the distinct geometry of
782 Late Mesozoic (Tier 1) and Paleogene (Tier 2) faults over Anticlines B and C. These two fault
783 tiers are separated by the Base Tertiary Unconformity (horizon H6). However, some of the
784 Tier 2 faults propagate downwards and offset horizon H6. The location of the seismic line is
785 shown in Figs. 1b, 10, 11 and 12.

786 **Fig. 6.** a) Uninterpreted and b) interpreted seismic profiles revealing the geometry of Upper
787 Mesozoic (Tier 1) and Paleogene (Tier 2) faults over Anticline A. Tier 1 faults were generated
788 by the local buckling and stretching of the anticline's outer-arc strata during the Late
789 Cretaceous-Paleogene tectonic inversion episodes. These faults were eroded and truncated at
790 the Base of Tertiary Unconformity (horizon H6), with some reactivating upwards into
791 Paleogene strata (Unit S7), linking with the overlying Tier 2 faults. The location of the seismic
792 line is shown in Figs. 1b, 10, 11 and 12.

793 **Fig. 7.** a) Uninterpreted and b) interpreted seismic profiles highlighting the geometry of Upper
794 Mesozoic (Tier 1) and Paleogene (Tier 2) faults over Anticline A. The imaged fault tiers are
795 separated by the Base of Tertiary Unconformity (horizon H6), with some of the Tier 1 faults
796 reactivating upwards into Paleogene strata (Unit S7), linking with Tier 2 faults. The location
797 of the seismic line is shown in Figs. 1b, 10, 11 and 12.

798 **Fig. 8.** a) Uninterpreted and b) interpreted seismic profiles highlighting the geometry of Upper
799 Mesozoic (Tier 1) and Paleogene (Tier 2) faults over Anticline A. Distinct fault tiers are
800 separated by the Base Tertiary Unconformity (H6), but with some of the Tier 1 faults
801 reactivating upwards into Paleogene strata (S7) to link with Tier 2 faults. A deeply rooted listric
802 fault that detaches on top Zechstein salt (H2) propagates vertically into Paleogene strata (S7).
803 Some of the Tiers 1 and 2 faults intersect this listric fault. The location of the seismic line is
804 shown in Figs. 1b, 10, 11 and 12.

Fig. 9. a) Uninterpreted and b) Interpreted inline seismic sections revealing the geometry of Tier 2 faults in Paleogene strata (Unit S7: Lower North Sea Group), c) Uninterpreted and d) Interpreted cross-line seismic sections also highlighting the geometry of Tier 2 faults in Paleogene strata. These faults are closely spaced, with some also segmented. They result from near-seafloor extension over growing anticlines and sudden compaction of mud-rich strata (with subsequent loss of volume and fluid), forming polygonal fault geometries. The location of the seismic lines are shown in Figs. 1b, 10, 11 and 12.

Fig. 10. a) TWTT structural map of a representative interval in Upper Mesozoic strata (H4a) highlighting the geometry of Tier 1 faults, the location of exploration wells and key seismic lines, b) Interpreted sketch highlighting the map view geometry of Tier 1 faults over the NW-SE trending Anticline A. These faults show linear to curvilinear geometries in map view. A, B and C are anticlines responding to the effect of tectonic inversion in the Southern North Sea.

Fig. 11. a) TWTT structural map for representative interval in Paleogene strata highlighting the geometry of Tier 2 faults, the location of exploration wells and key seismic lines, b) Interpreted sketch highlighting the geometry of Tier 2 faults. A, B and C are anticlines responding to the effect of tectonic inversion in the Southern North Sea.

Fig. 12. a) TWTT structural map of the Base Tertiary Unconformity (horizon H6) highlighting the location of exploration wells and key seismic lines. A, B and C are anticlines responding to the effect of tectonic inversion in the Southern North Sea, b) Interpreted sketch highlighting the geometry of reactivated fault families affecting the Base Tertiary Unconformity (horizon H6). Reactivated Tier 1 faults show linear to curvilinear geometries around Anticline A. Tier 2 faults show irregular polygonal geometries over Anticlines B and C.

Fig. 13. a) Uninterpreted and b) interpreted seismic profiles revealing the geometry of representative Upper Mesozoic (Tier 1) faults over Anticline A. These faults were eroded and

truncated at the Base of Tertiary Unconformity (non-reactivated Tier 1 faults), with some reactivating and propagating upwards into Paleogene strata (Reactivated Tier 1 faults). The location of the seismic line is shown in Figs. 1b, 10, 11 and 12.

Fig. 14. a) Uninterpreted and b) interpreted seismic profiles revealing the geometry of representative Upper Mesozoic (Tier 1) faults over Anticline A. These faults were eroded and truncated at the Base of Tertiary Unconformity (non-reactivated Tier 1 faults), with some reactivating and propagating upward into Paleogene strata (Reactivated Tier 1 faults). Some of the Tier 1 faults intersect a deeply rooted listric fault that detaches on the top of Zechstein salt.

Fig. 15. Representative throw-depth (T-Z) profiles stressing the influence of mechanical stratigraphy and lithology on throw distribution and growth in fault F1. a) Interpreted seismic section and well log. b) Representative throw-depth (T-Z) profiles revealing fault reactivation and growth by segment linkage. Here, two separate pre-existing faults with throw maxima in sand-rich competent intervals have propagated towards each other and linked in shale-rich intervals, where local fault throw minima are recorded. c) Throw-depth contour map showing anomalous throw distributions and, d) Throw-distance (T-X) plots through the contour map. See Fig. 13 for a full seismic section of the interpreted fault F1.

Fig. 16. Representative throw-depth (T-Z) profiles revealing the effect of mechanical stratigraphy and lithology on throw distribution and growth in fault F2. a) Interpreted seismic section and well log. b) Representative throw-depth (T-Z) profiles showing fault reactivation and growth by segment linkage. Two separate faults with local throw maxima between 15 and 30 ms (18.2-37.8 m) in sand-rich (competent) intervals have propagated towards each other and linked in shale-rich (incompetent) intervals, where local throw minima between 2 and 15 ms (2.5-19.2 m) are recorded. c) Throw-depth contour map showing anomalous throw

852 distributions. d) Throw-distance (T-X) plots through the contour map stressing fault growth
853 via segment linkage. See Fig. 13 for a full seismic section of the interpreted fault F2.

854 **Fig. 17.** Representative throw-depth (T-Z) profiles revealing the effect of mechanical
855 stratigraphy and lithology on throw distribution and growth in fault F3. In sand-rich intervals,
856 fault throws are usually larger - between 14 and 30 ms (17.7-37.8 m) - compared to the smaller
857 fault throws between 2 and 14 ms (2.5-17.7 m) recorded in shale rich-intervals. These changes
858 in throw values are interpreted to be a consequence of mechanical stratigraphy and lithological
859 changes in the host rock. a) Interpreted seismic section and well log. b) Representative throw-
860 depth (T-Z) profiles showing fault reactivation and growth by segment linkage. c) Throw-depth
861 contour map showing throw distributions. d) Throw-distance (T-X) plots through the contour
862 map. See Fig. 13 for a full seismic section of the interpreted fault F3.

863 **Fig. 18.** Representative throw-depth (T-Z) profiles stressing the influence of mechanical
864 stratigraphy and lithology on throw distribution and growth in fault F4. A reduction in throw
865 values is observed as faults propagate from sand-rich intervals into shale-rich intervals. a)
866 Interpreted seismic section and well log. b) Representative throw-depth (T-Z) profiles
867 highlighting the fault reactivation and growth by segment linkage, where two separate pre-
868 existing faults with throw maxima in sand-rich competent intervals have propagated towards
869 each other and linked in shale-rich intervals, where local fault throw minima are recorded. c)
870 Throw-depth contour map showing throw distributions. d) Throw-distance (T-X) plots through
871 the contour map. See Fig. 14 for a full seismic section of the interpreted fault F4.

872 **Fig. 19.** Representative throw-depth (T-Z) profiles revealing the effect of mechanical
873 stratigraphy and lithology on throw distribution and growth in fault F5. a) Interpreted seismic
874 section and well log. b) Representative throw-depth (T-Z) profiles highlighting fault
875 reactivation and growth by segment linkage. c) Throw-depth contour map showing anomalous

throw distributions. d) Throw-distance (T-X) plots through the contour map stressing fault growth via segment linkage. See Fig. 14 for a full seismic section of the interpreted fault F5.

Fig. 20. Representative throw-depth (T-Z) profiles revealing the effect of mechanical stratigraphy and lithology on throw distribution and growth on fault F6. a) Interpreted seismic section and well log. b) Representative throw-depth (T-Z) profiles highlighting fault reactivation and growth by segment linkage. Here, two separate pre-existing faults with throw maxima in more competent intervals have propagated towards each other and linked in less competent intervals. c) Throw-depth contour map showing throw distributions. d) Throw-distance (T-X) plots through the contour map. See Figs. 6 and 7 for a full seismic section of the interpreted fault F6.

Fig. 21. Representative throw-depth (T-Z) profiles for a listric fault showing typical growth by upwards propagation i.e. a vertical, positive stepped throw gradient. The decrease and vertical positive step in throw gradients recorded by the listric fault can be related to the effects of reactivation by upwards propagation from parent faults above a detachment surface, i.e. Zechstein salt in Fig. 6.

Fig. 22. a) Uninterpreted and b) interpreted seismic profiles showing the geometry of Tier 2 faults in Paleogene strata (Unit S7; Lower North Sea Group). c) Representative throw-depth (T-Z) profiles highlighting the reactivation and growth history of Tier 2 faults. The sharp changes in throw values are interpreted to relate to fault reactivation and growth by segment linkage, where multiple throw maxima are separated by throw minima.

Fig. 23. Schematic illustration of the relative age and time-span of representative distinct fault tiers mapped over the NW-SE striking Anticline A. Plotted in the diagram is the number of reflections affected by faults above and below the Base Tertiary Unconformity (H6). Tier 1 faults dominantly offset Upper Mesozoic strata and truncated/eroded at the Base Tertiary

Unconformity (Non-reactivated Tier 1 faults), with some faults reactivating upwards into Paleogene strata (Reactivated Tier 1 faults). Tier 2 faults dominantly offset Paleogene strata. They are related to early diagenesis but still record the effect of the Paleogene inversion episode. Main stratigraphic groups, tectonic phases and unconformities related to regional tectonic events are based on Penge et al. (1999) and van Verweij and Simmelink (2002).

Fig. 24. Schematic model for the geological evolution of the study area highlighting the age and reactivation of main fault families. Listric faults were active during the Jurassic syn-rift phase in association with rift-raft tectonics, b). c) Tier 1 faults occurred during Late Cretaceous Sub-Hercynian inversion, i.e. the time of the formation of major anticlines and deposition of the Chalk Group. d) Period of reactivation of Sub-Hercynian faults (Tier 1 faults) and erosion of their upper fault tips by the Paleocene-Laramide erosional event, creating a prominent Late Cretaceous-Tertiary Unconformity (horizon H6). e) Phase of reactivation of some Tier 1 faults into the Paleogene strata during Oligocene-Pyrenian inversion and formation of Tier 2 faults in Paleogene strata. The present-day, post-inversion phase comprises two distinct fault tiers: Tier 1 (Late Mesozoic) and Tier 2 (Paleogene) faults.

List of Figures

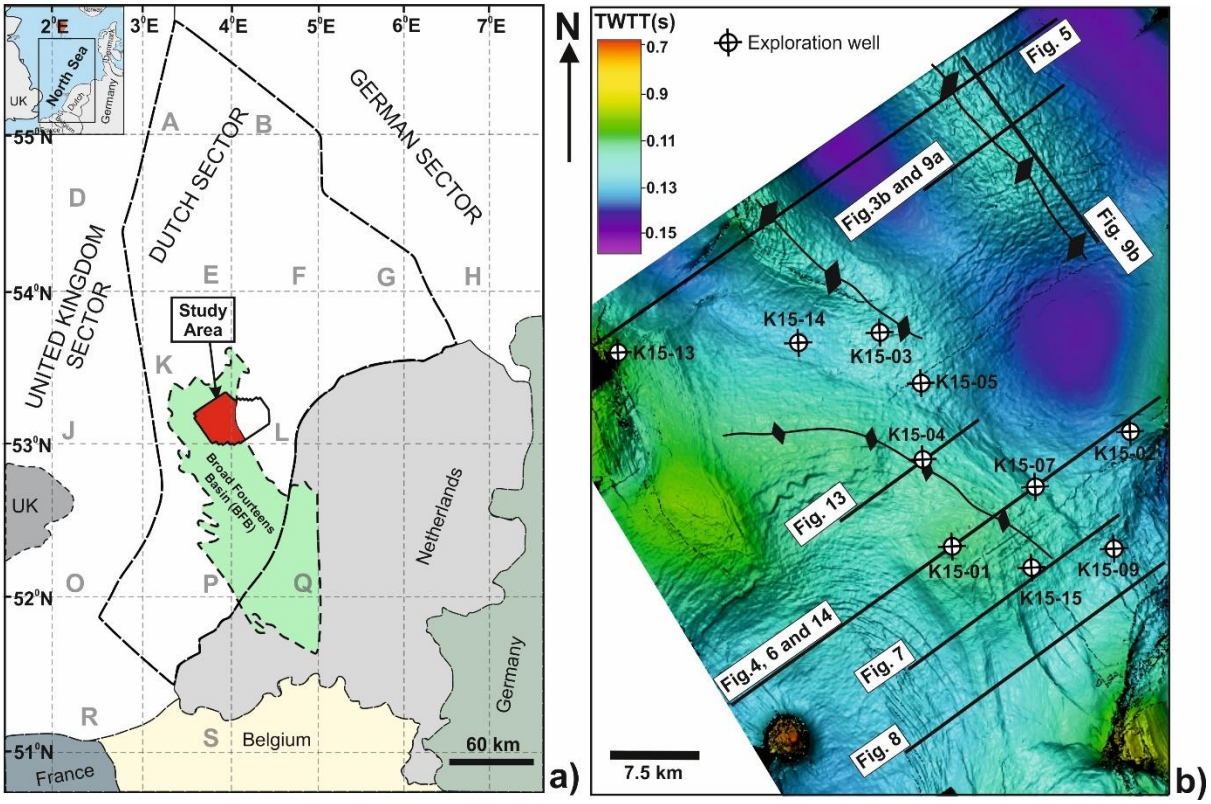

Fig. 1

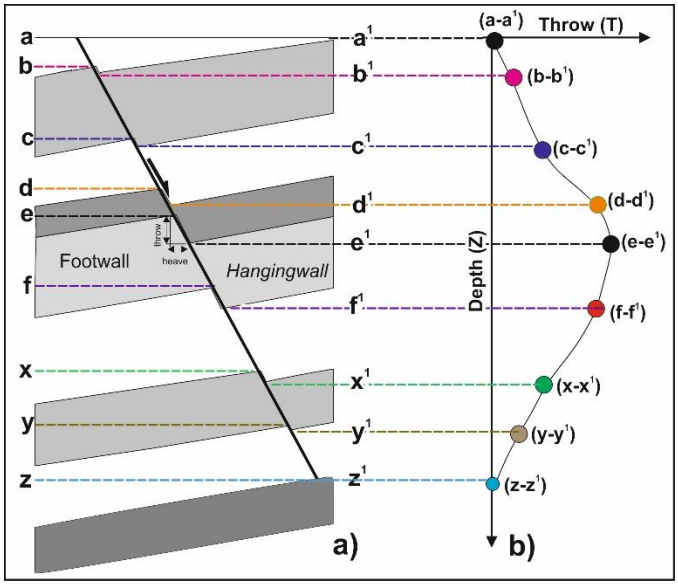
a
b
c
d
e
f
x
y
z
Footwall
Hangingwall
throw
heave
a1
b1
c1
d1
e1
f1
x1
y1
z1
(a-a1)
Throw (T)
(b-b1)
(c-c1)
(d-d1)
(e-e1)
(f-f1)
(x-x1)
(y-y1)
(z-z1)
Depth (Z)
a)
b)

Fig. 2

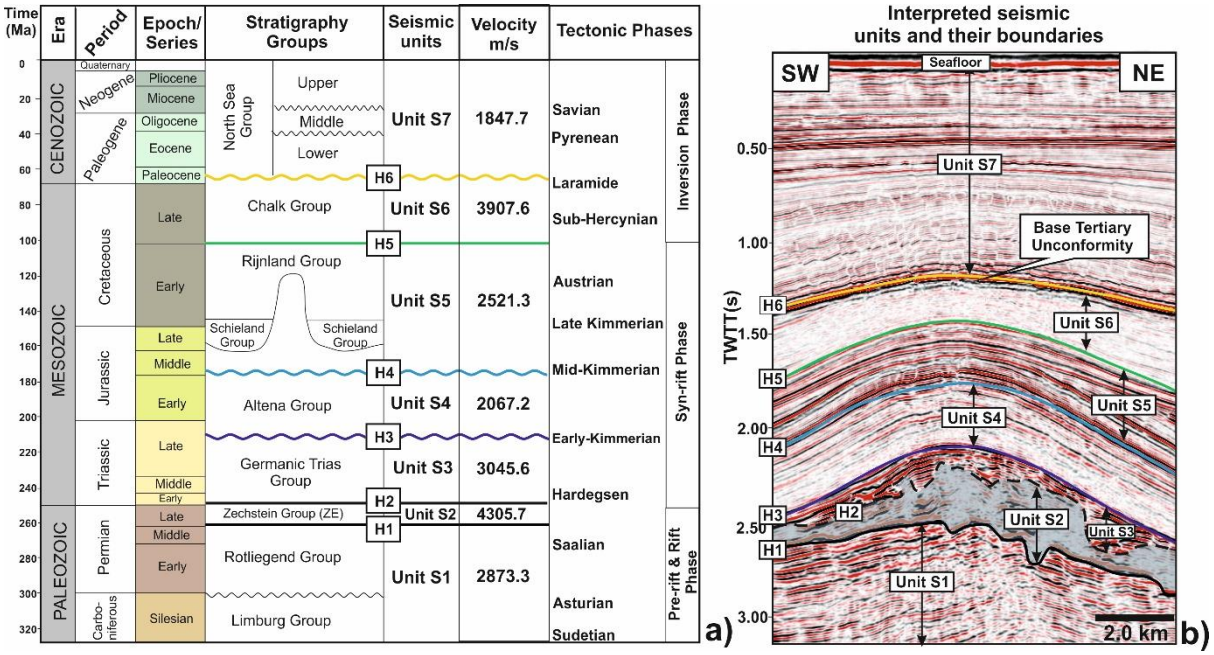
Time (Ma)
Era
Period
Epoch/ Series
Stratigraphy Groups
Seismic units
Velocity m/s
Tectonic Phases
CENOZOIC
MESOZOIC
PALEOZOIC
Quaternary
Neogene
Paleogene
Cretaceous
Jurassic
Triassic
Permian
Carbo-niferous
Pliocene
Miocene
Oligocene
Eocene
Paleocene
Late
Early
Middle
Silesian
North Sea Group
Upper
Middle
Lower
Chalk Group
Rijnland Group
Schieland Group
Altena Group
Germanic Trias Group
Zechstein Group (ZE)
Rotliegend Group
Limburg Group
H6
H5
H4
H3
H2
H1
Unit S7
Unit S6
Unit S5
Unit S4
Unit S3
Unit S2
Unit S1
1847.7
3907.6
2521.3
2067.2
3045.6
4305.7
2873.7
Savian
Pyrenean
Laramide
Sub-Hercynian
Austrian
Late Kimmerian
Mid-Kimmerian
Early-Kimmerian
Hardegsen
Saalian
Asturian
Sudetian
Inversion Phase
Syn-rift Phase
Pre-rift & Rift Phase
a)
Interpreted seismic units and their boundaries
SW
NE
Seafloor
Unit S7
Base Tertiary Unconformity
Unit S6
Unit S5
Unit S4
Unit S3
Unit S2
Unit S1
TWTT (s)
0.50
1.00
1.50
2.00
2.50
3.00
2,0 km
b)

Fig. 3

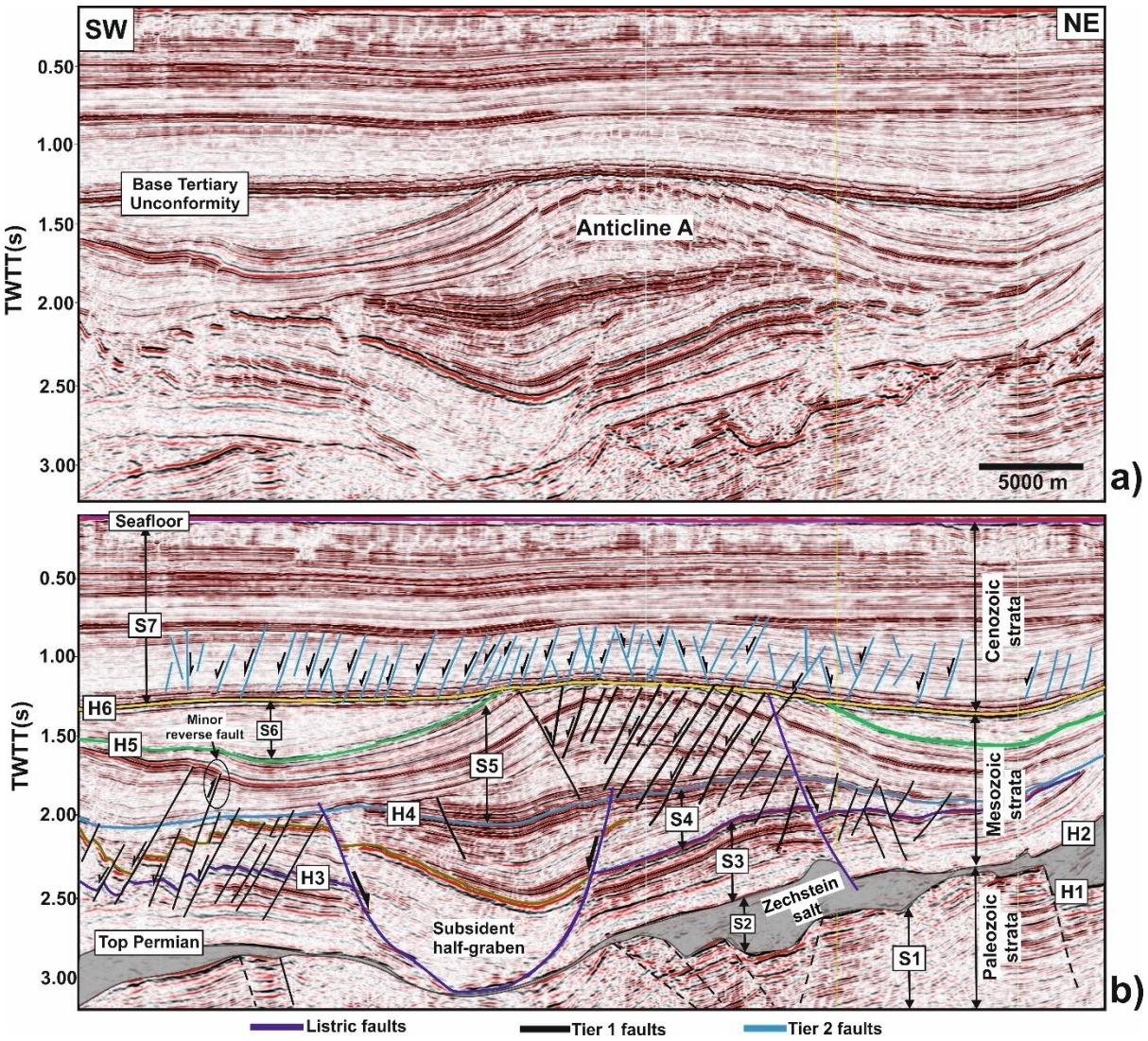
SW
NE
TWTT(s)
0.50
1.00
1.50
2.00
2.50
3.00
Base Tertiary Unconformity
Anticline A
5000 m
a)
Seafloor
S7
H6
H5
Minor reverse fault
S6
S5
H4
H3
S4
S3
S2
S1
Zechstein salt
Subsident half-graben
Top Permian
H2
H1
Cenozoic strata
Mesozoic strata
Paleozoic strata
b)
Listric faults
Tier 1 faults
Tier 2 faults

Fig. 4

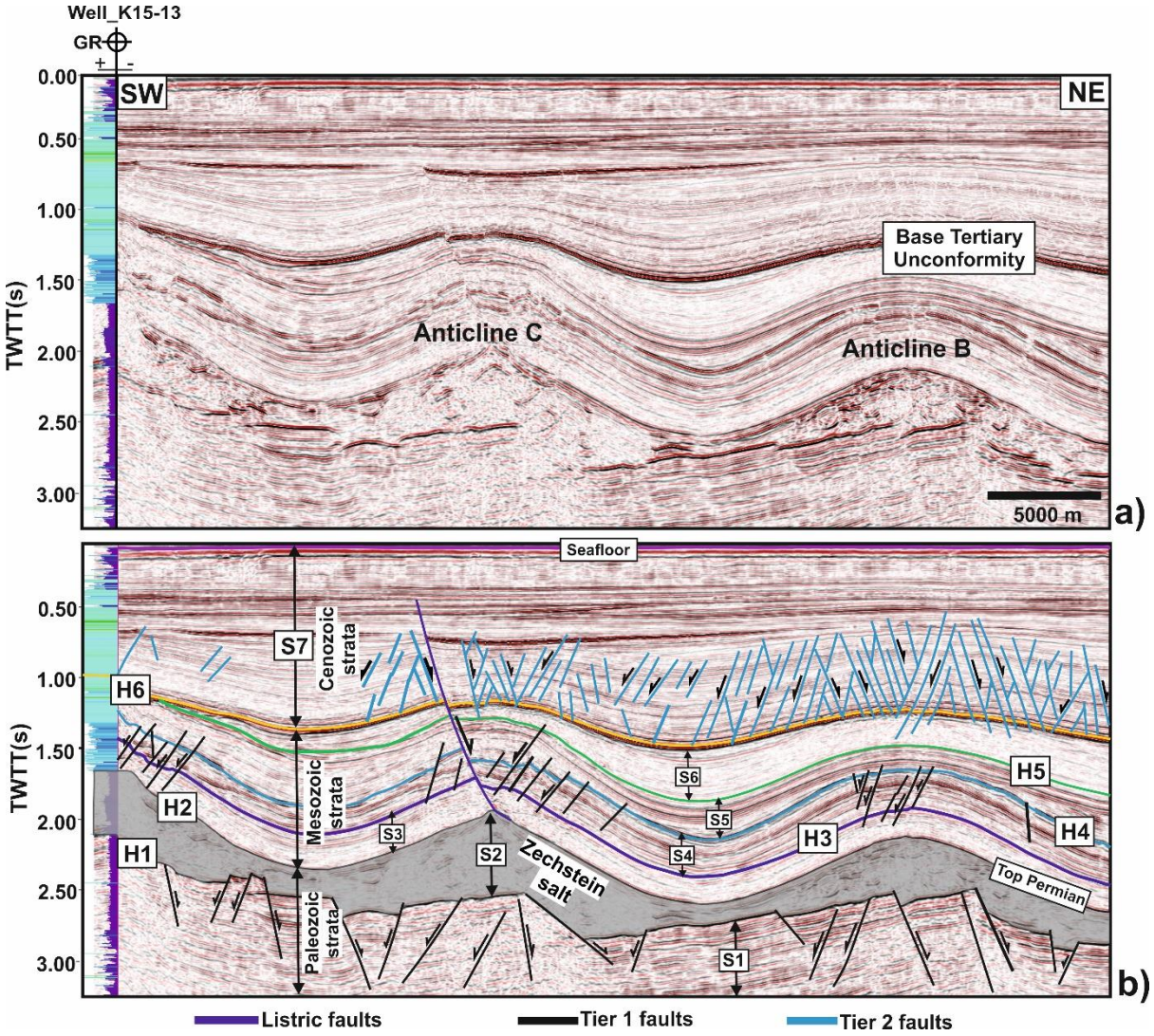
Well_K15-13
GR
SW
NE
TWTT(s)
0.00
0.50
1.00
1.50
2.00
2.50
3.00
Base Tertiary Unconformity
Anticline C
Anticline B
5000 m
a)
Seafloor
S7
Cenozoic strata
H6
H2
H1
Mesozoic strata
Paleozoic strata
S3
S2
Zechstein salt
S6
S5
S4
H3
H5
H4
Top Permian
S1
b)
Listric faults
Tier 1 faults
Tier 2 faults

Fig. 5

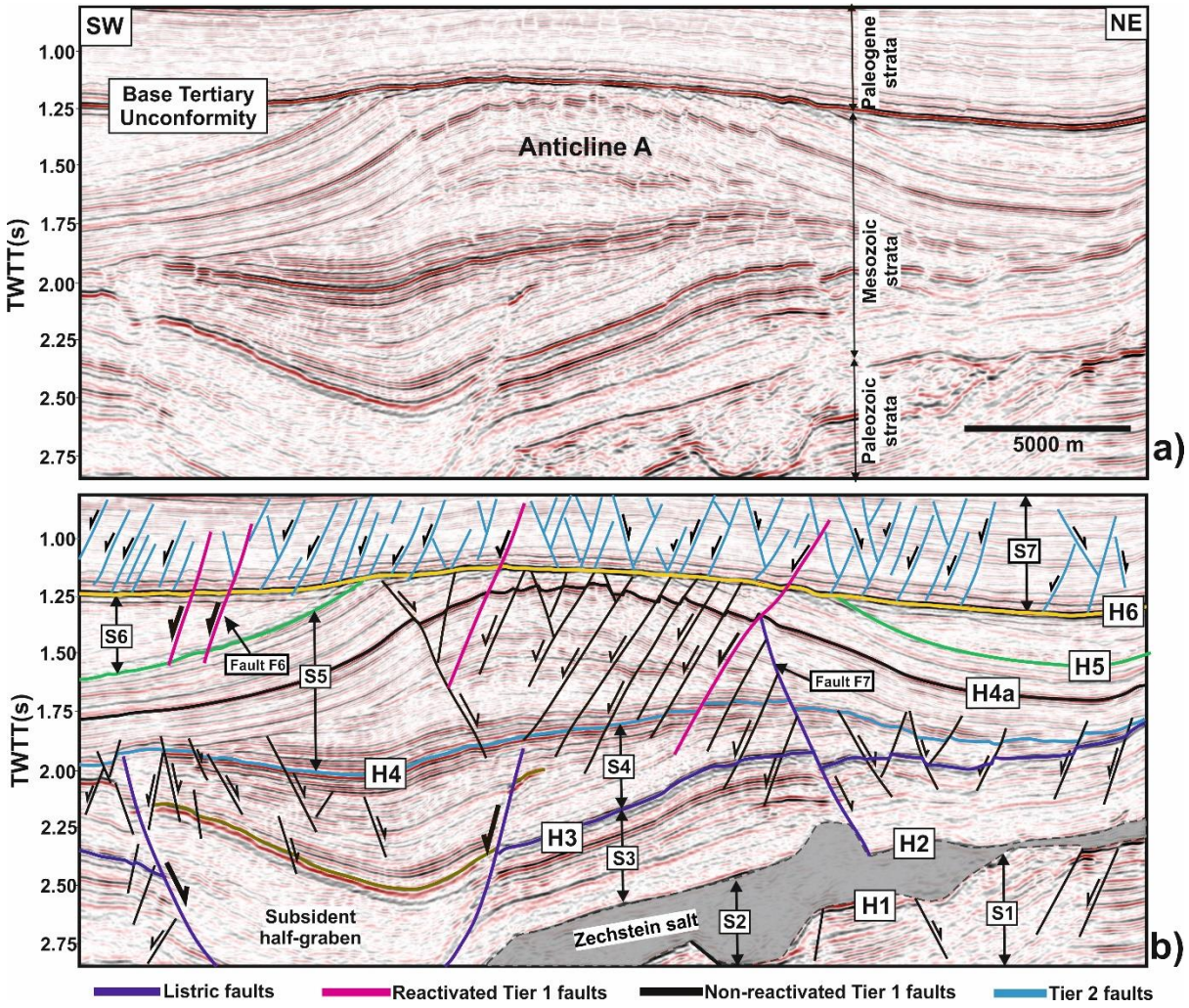
SW
NE
Base Tertiary Unconformity
Anticline A
Paleogene strata
Mesozoic strata
Paleozoic strata
5000 m
a)
TWTT(s)
1.00
1.25
1.50
1.75
2.00
2.25
2.50
2.75
S7
H6
S6
Fault F6
S5
H5
Fault F7
H4a
H4
S4
H3
S3
H2
S2
H1
S1
Subsident half-graben
Zechstein salt
b)
Listric faults
Reactivated Tier 1 faults
Non-reactivated Tier 1 faults
Tier 2 faults

Fig. 6

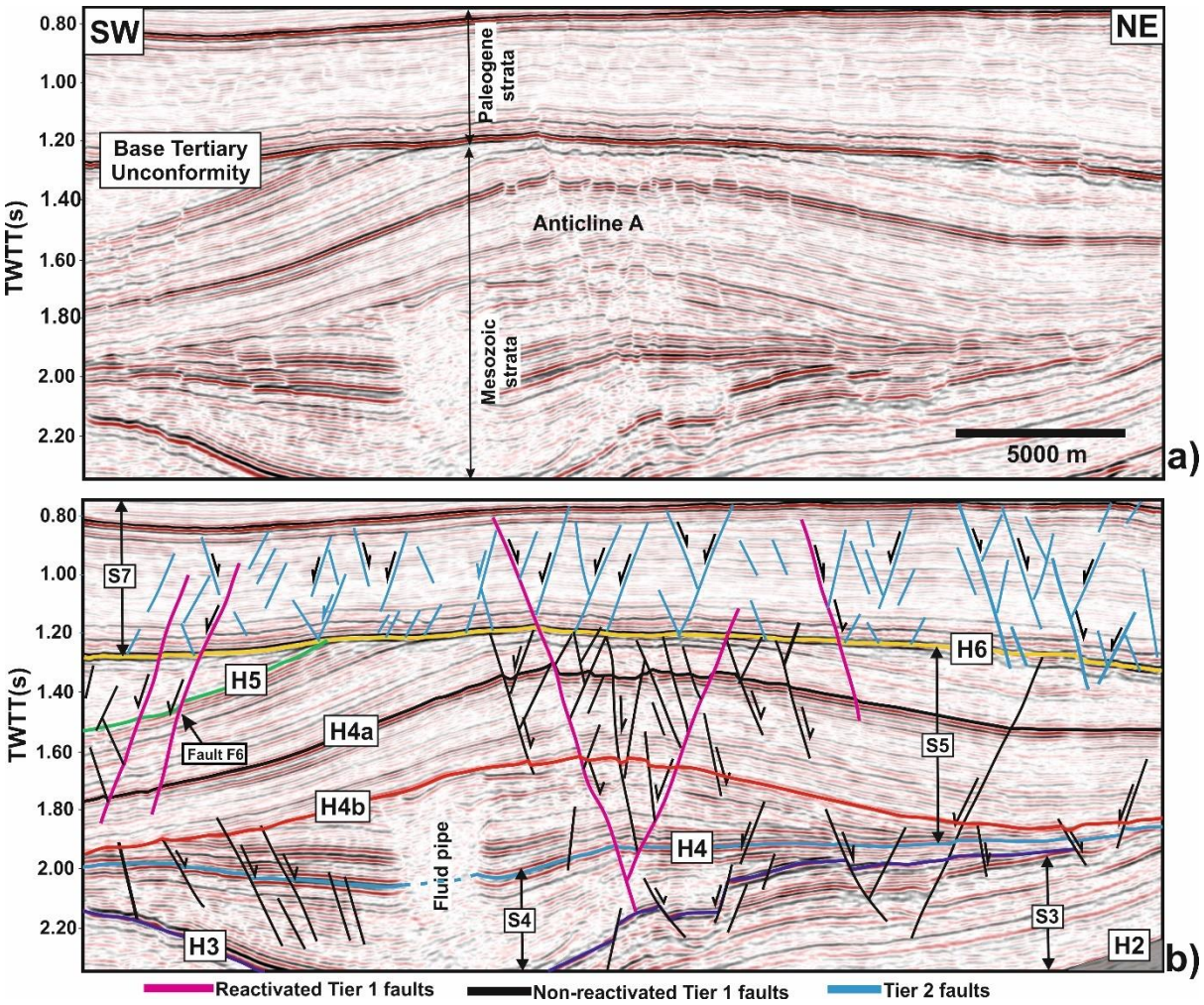
SW
NE
0.80
1.00
1.20
1.40
1.60
1.80
2.00
2.20
TWTT(s)
Base Tertiary Unconformity
Paleogene strata
Anticline A
Mesozoic strata
5000 m
a)
S7
H5
H4a
Fault F6
H4b
Fluid pipe
H4
H6
S5
S4
S3
H3
H2
b)
Reactivated Tier 1 faults
Non-reactivated Tier 1 faults
Tier 2 faults

Fig. 7

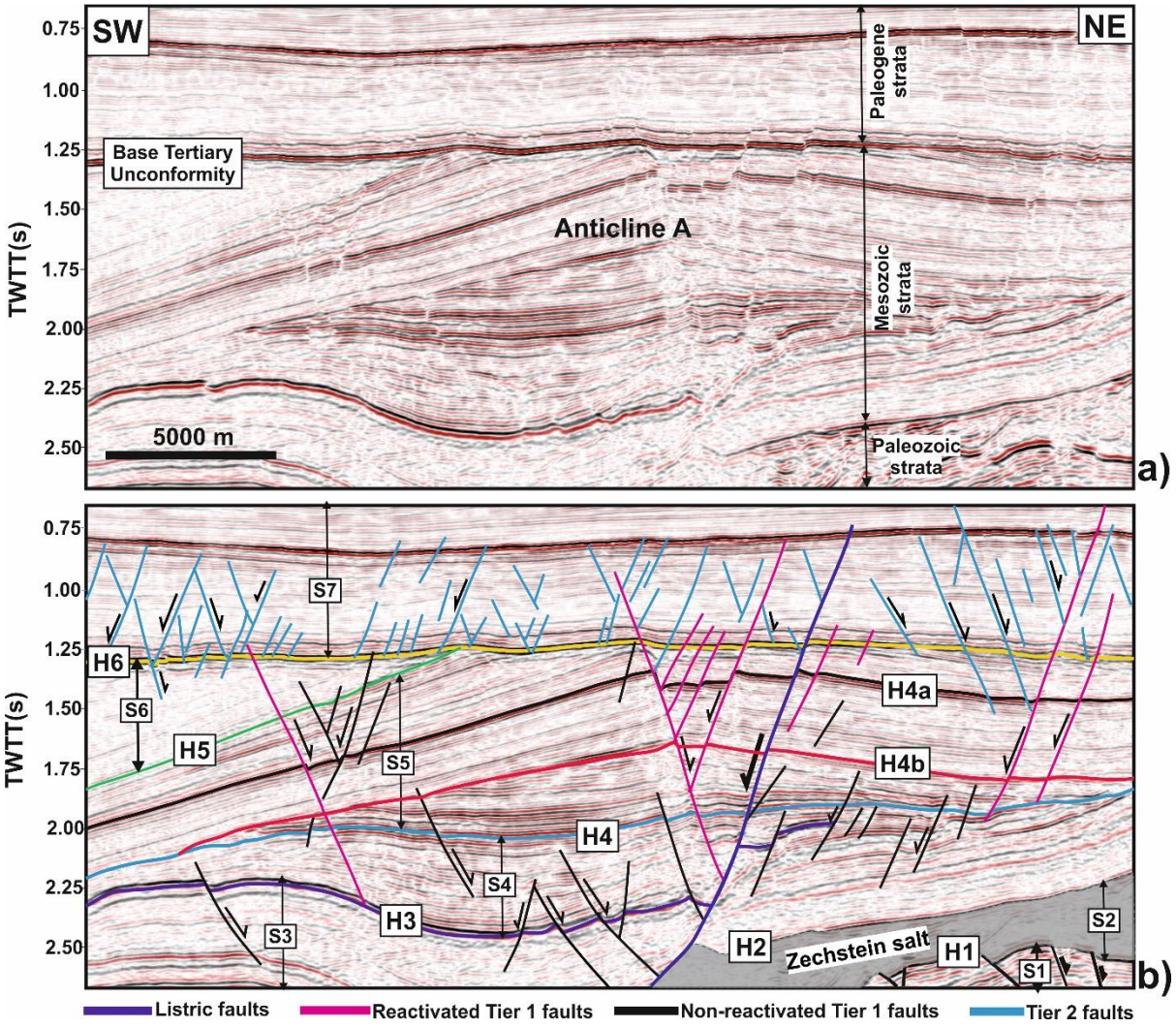
SW
NE
Base Tertiary Unconformity
Anticline A
Paleogene strata
Mesozoic strata
Paleozoic strata
5000 m
TWTT(s)
0.75
1.00
1.25
1.50
1.75
2.00
2.25
2.50
a)
S7
H6
S6
H5
S5
H4a
H4b
H4
S4
H3
S3
H2
Zechstein salt
H1
S2
S1
b)
Listric faults
Reactivated Tier 1 faults
Non-reactivated Tier 1 faults
Tier 2 faults

Fig. 8

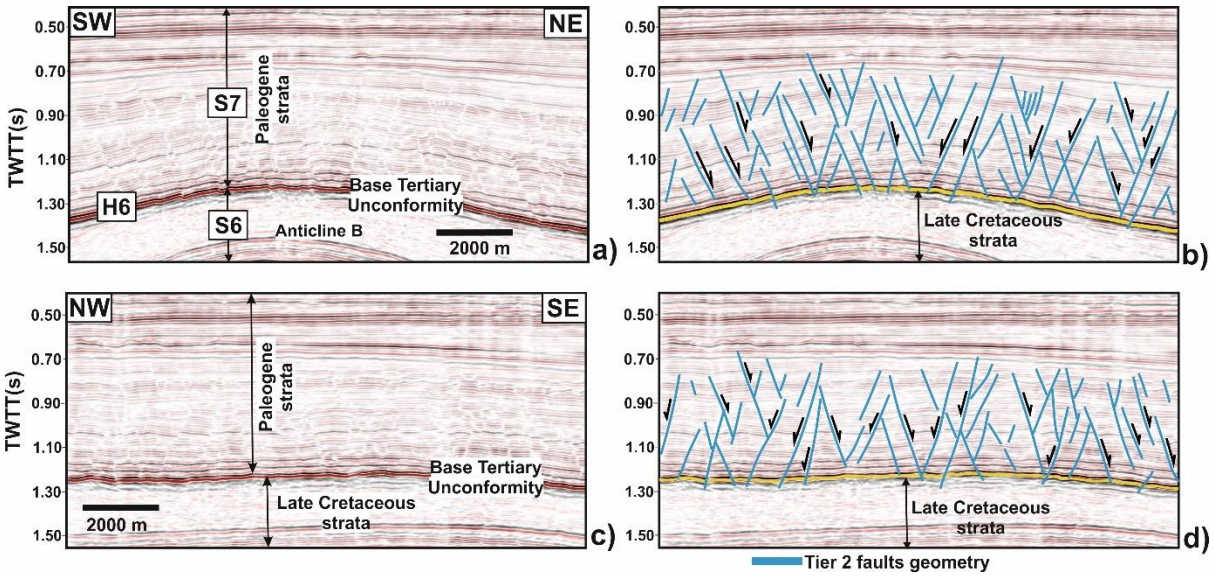
SW
NE
TWTT(s)
0.50
0.70
0.90
1.10
1.30
1.50
S7
Paleogene strata
H6
S6
Base Tertiary Unconformity
Anticline B
2000 m
a)
Late Cretaceous strata
b)
NW
SE
Paleogene strata
Base Tertiary Unconformity
Late Cretaceous strata
2000 m
c)
Late Cretaceous strata
d)
Tier 2 faults geometry

Fig. 9

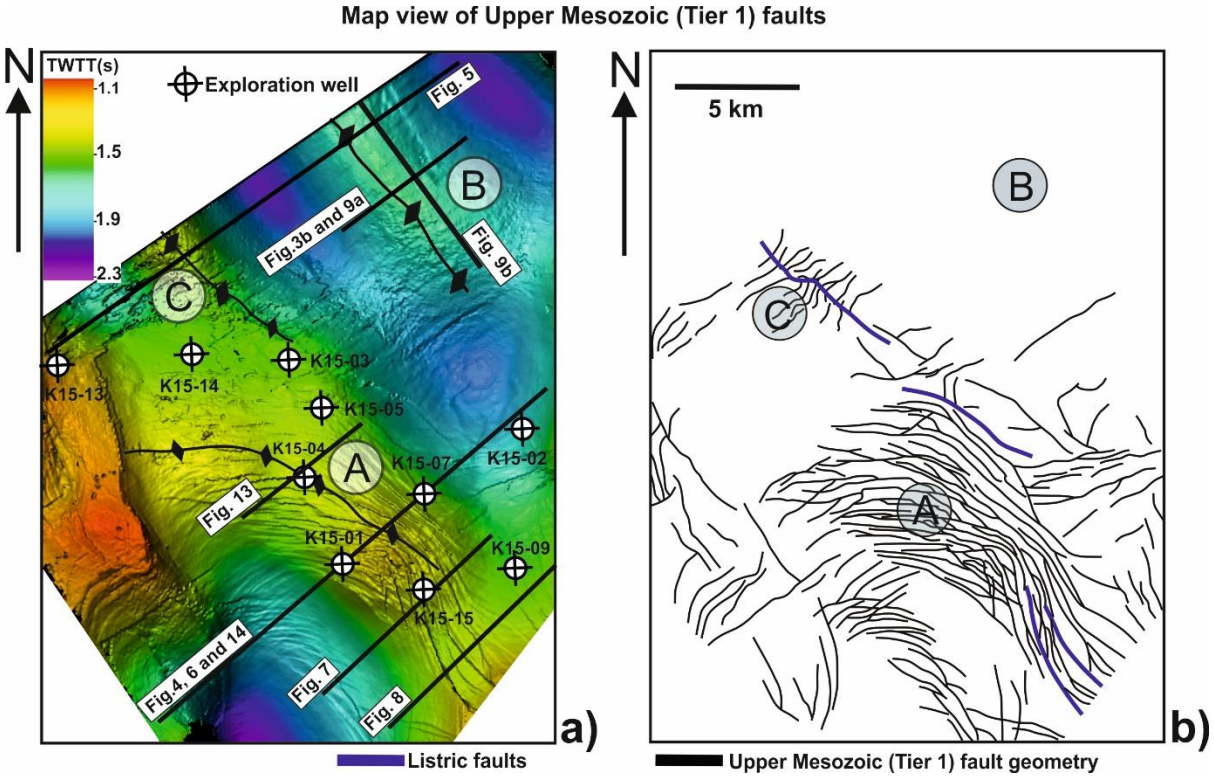
Map view of Upper Mesozoic (Tier 1) faults
N
TWTT(s)
1.1
1.5
1.9
2.3
Exploration well
Fig. 5
Fig.3b and 9a
Fig. 9b
B
C
A
K15-13
K15-14
K15-03
K15-05
K15-04
K15-07
K15-02
Fig. 13
K15-01
K15-09
K15-15
Fig.4, 6 and 14
Fig. 7
Fig. 8
a)
Listric faults
N
5 km
B
C
A
b)
Upper Mesozoic (Tier 1) fault geometry

Fig. 10

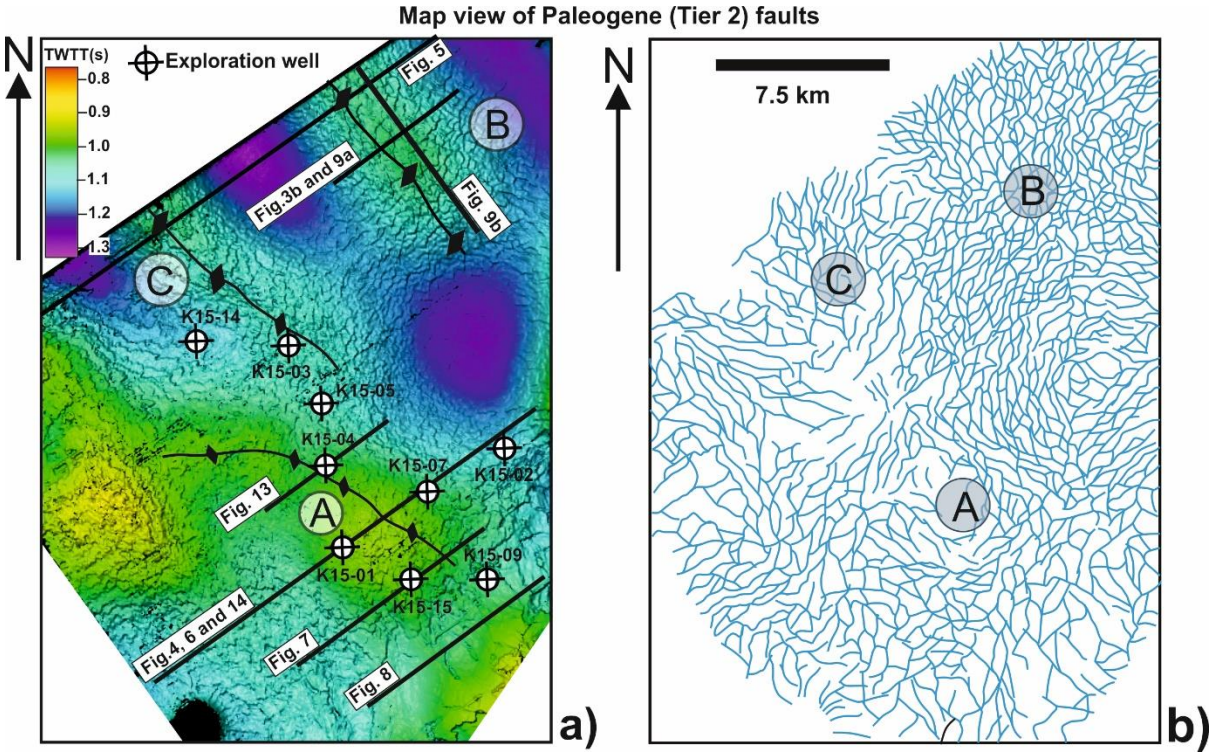
Map view of Paleogene (Tier 2) faults
N
TWTT(s)
0.8
0.9
1.0
1.1
1.2
1.3
Exploration well
Fig. 5
Fig.3b and 9a
Fig. 9b
B
C
K15-14
K15-03
K15-05
K15-04
K15-07
K15-02
Fig. 13
A
K15-01
K15-09
K15-15
Fig.4, 6 and 14
Fig. 7
Fig. 8
a)
N
7.5 km
B
C
A
b)

Fig. 11

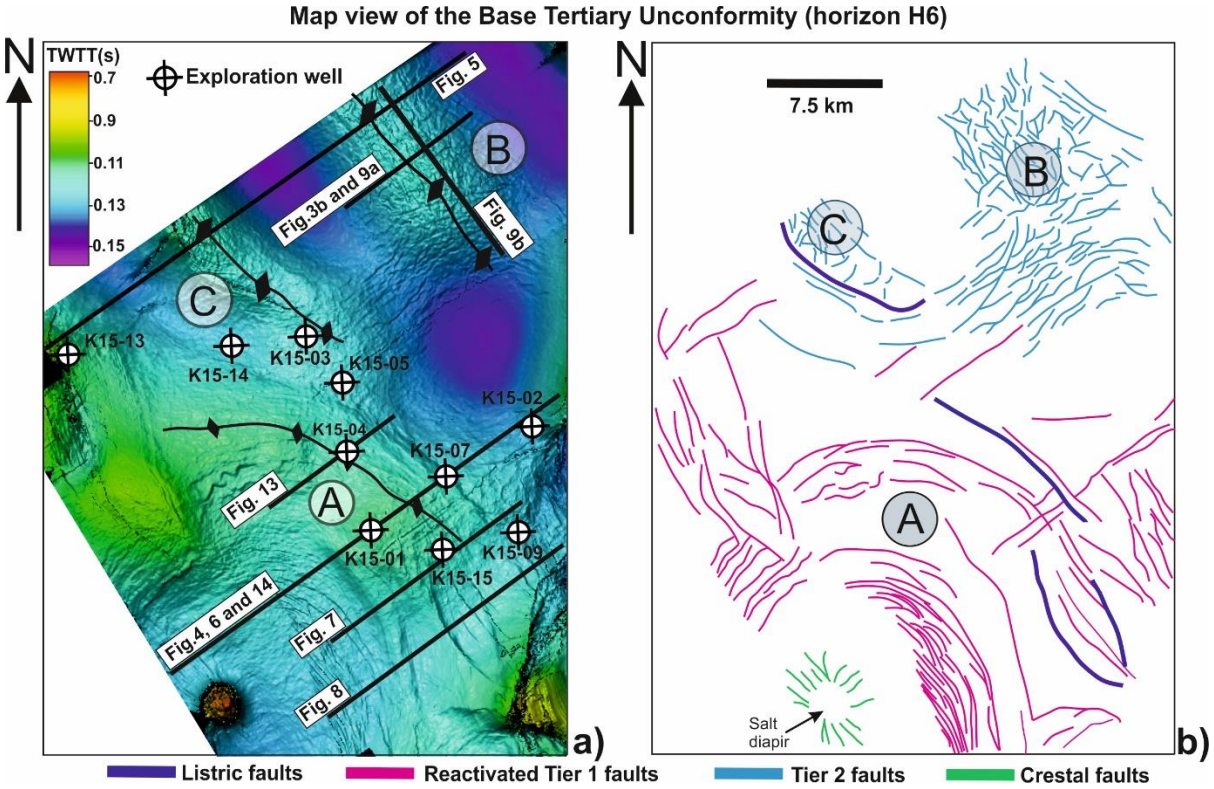
Map view of the Base Tertiary Unconformity (horizon H6)
N
TWTT(s)
0.7
0.9
0.11
0.13
0.15
Exploration well
Fig. 5
Fig.3b and 9a
Fig. 9b
B
C
A
K15-13
K15-14
K15-03
K15-05
K15-02
K15-04
K15-07
Fig. 13
K15-01
K15-15
K15-09
Fig.4, 6 and 14
Fig. 7
Fig. 8
a)
N
7.5 km
B
C
A
Salt diapir
b)
Listric faults
Reactivated Tier 1 faults
Tier 2 faults
Crestal faults

Fig. 12

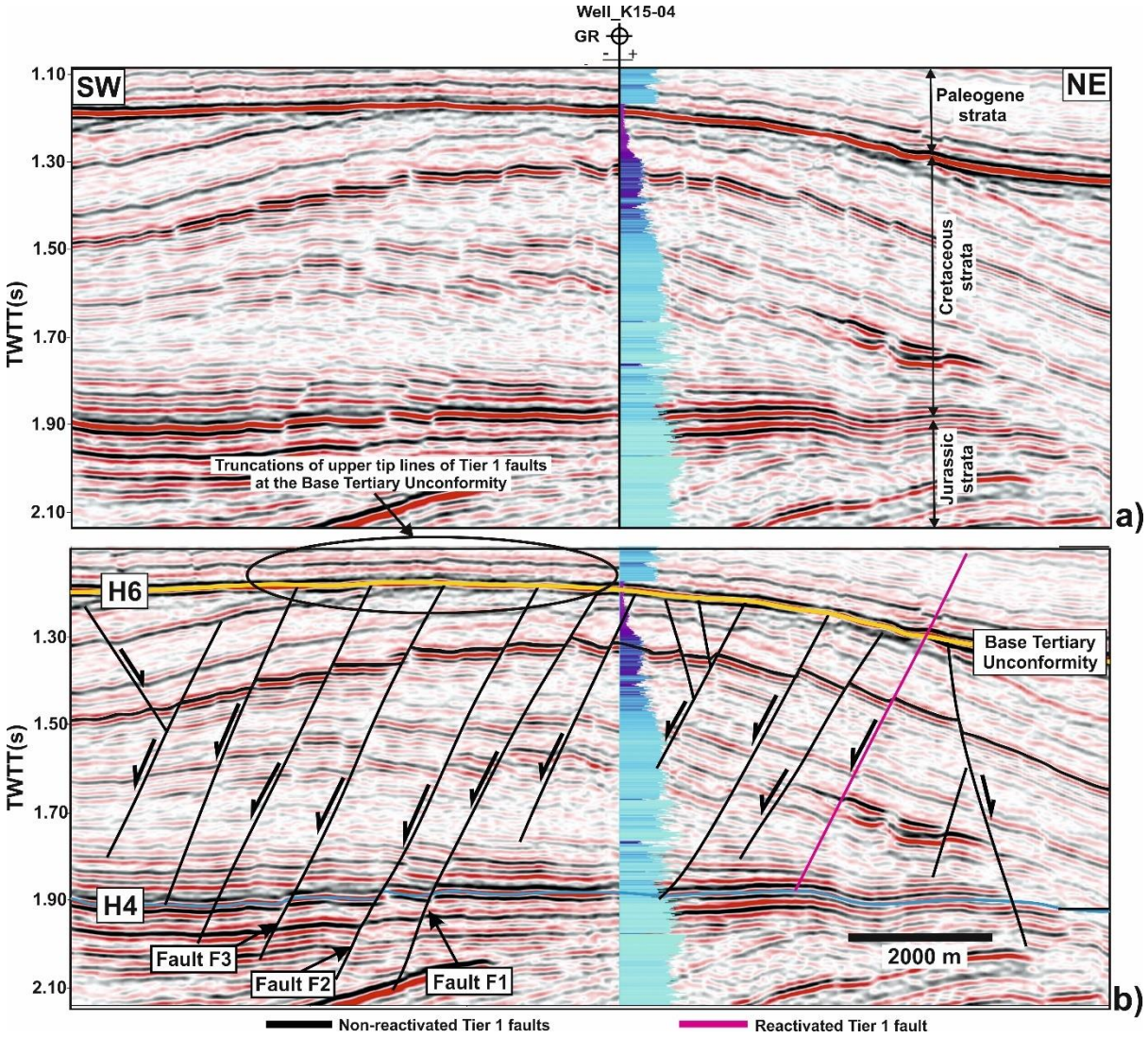
Well_K15-04
GR
SW
NE
Paleogene strata
Cretaceous strata
Jurassic strata
Truncations of upper tip lines of Tier 1 faults at the Base Tertiary Unconformity
TWTT(s)
1.10
1.30
1.50
1.70
1.90
2.10
a)
H6
H4
Base Tertiary Unconformity
Fault F3
Fault F2
Fault F1
2000 m
b)
Non-reactivated Tier 1 faults
Reactivated Tier 1 fault

Fig. 13

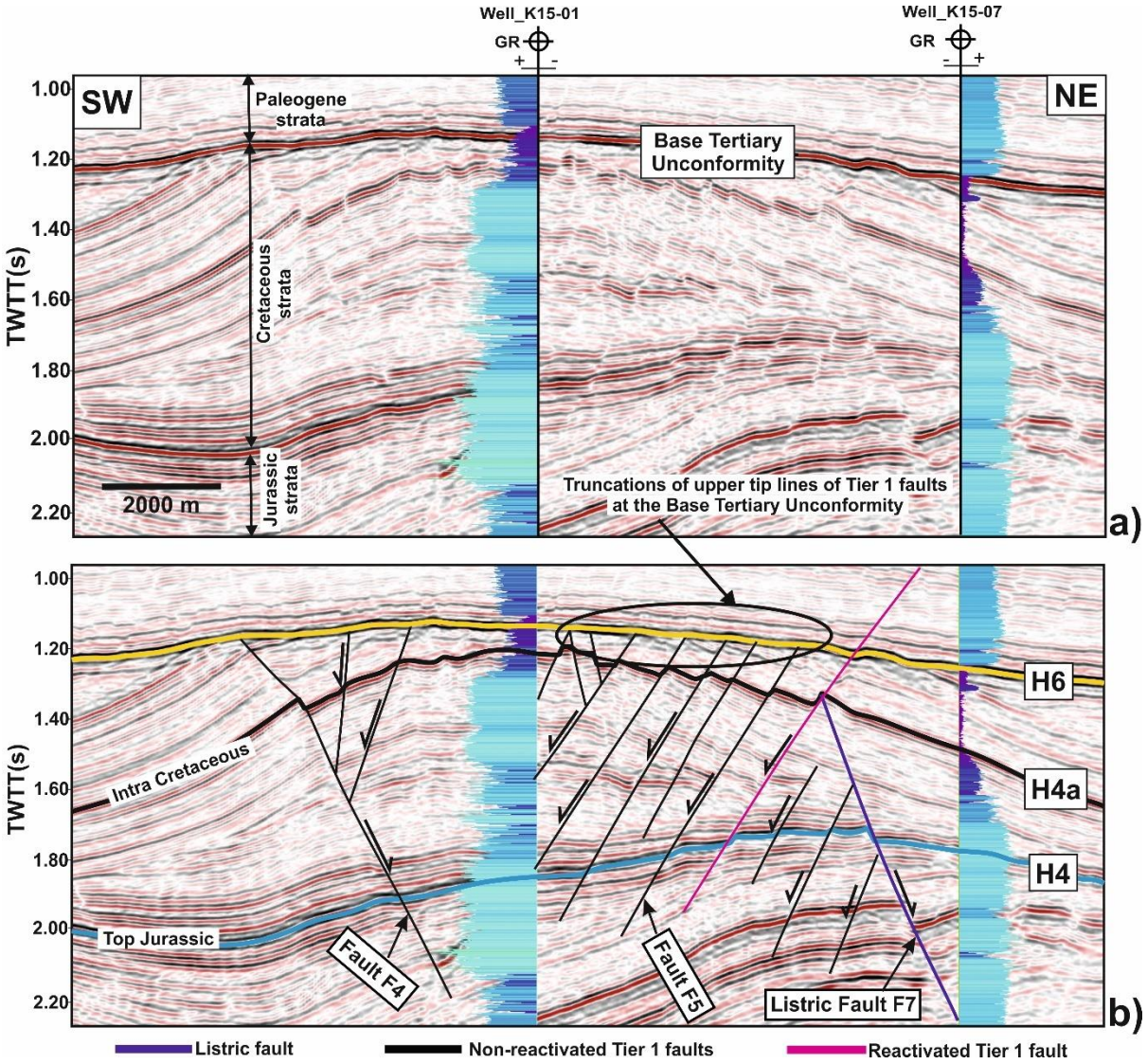
Well_K15-01
GR
Well_K15-07
GR
SW
NE
Paleogene strata
Cretaceous strata
Jurassic strata
Base Tertiary Unconformity
2000 m
TWTT(s)
1.00
1.20
1.40
1.60
1.80
2.00
2.20
Truncations of upper tip lines of Tier 1 faults at the Base Tertiary Unconformity
a)
Intra Cretaceous
Top Jurassic
Fault F4
Fault F5
Listric Fault F7
H6
H4a
H4
b)
Listric fault
Non-reactivated Tier 1 faults
Reactivated Tier 1 fault

Fig. 14

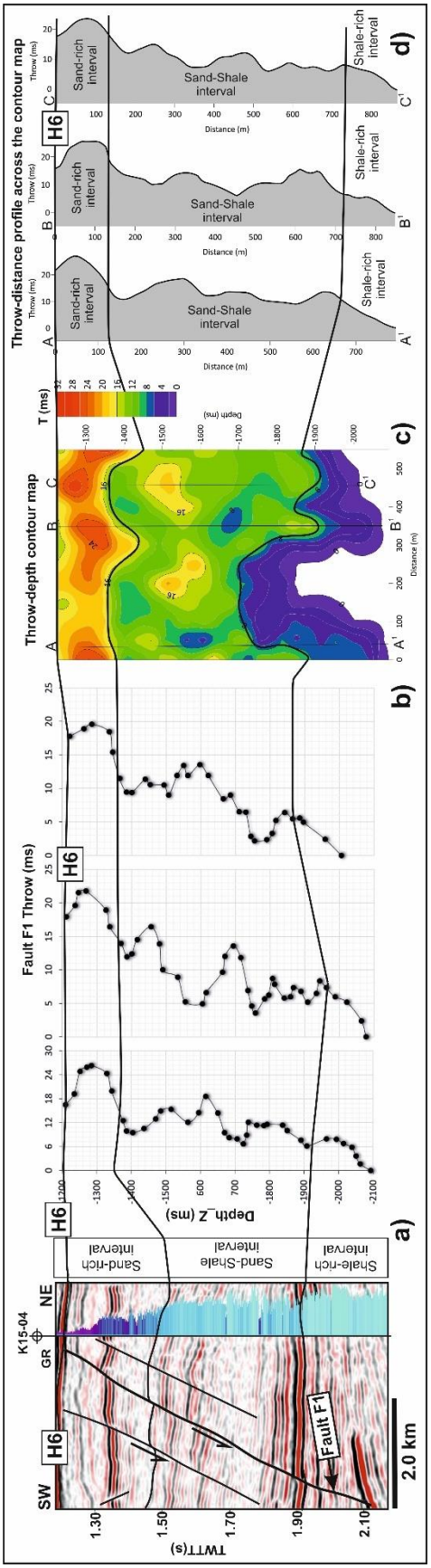
Correlation panel amongst fault throw distribution, lithology, and growth history for fault F1
a)
b)
c)
d)
H6
SW
NE
K15-04
GR
Fault F1
2.0 km
TWTT(s)
Depth_Z (ms)
Fault F1 Throw (ms)
Sand-rich interval
Sand-Shale interval
Shale-rich interval
Throw-depth contour map
Throw-distance profile across the contour map
Distance (m)
Throw (ms)
T (ms)
Depth (ms)

Fig. 15

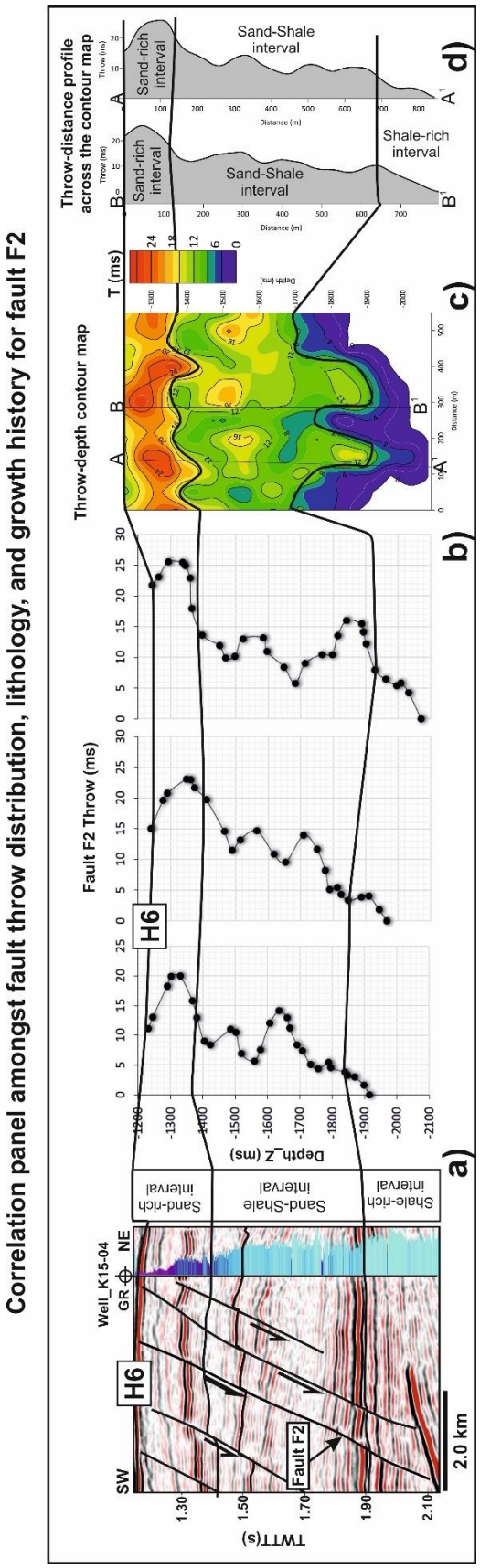
Correlation panel amongst fault throw distribution, lithology, and growth history for fault F2
a)
b)
c)
d)
Shale-rich interval
Sand-Shale interval
Sand-rich interval
Depth_Z (ms)
Fault F2 Throw (ms)
H6
Well_K15-04
GR
NE
SW
Fault F2
2.0 km
TWTT(s)
Throw-depth contour map
T (ms)
Throw-distance profile across the contour map
Sand-Shale interval
Shale-rich interval
Sand-rich interval
Distance (m)
Throw (ms)
Depth (ms)

Fig. 16

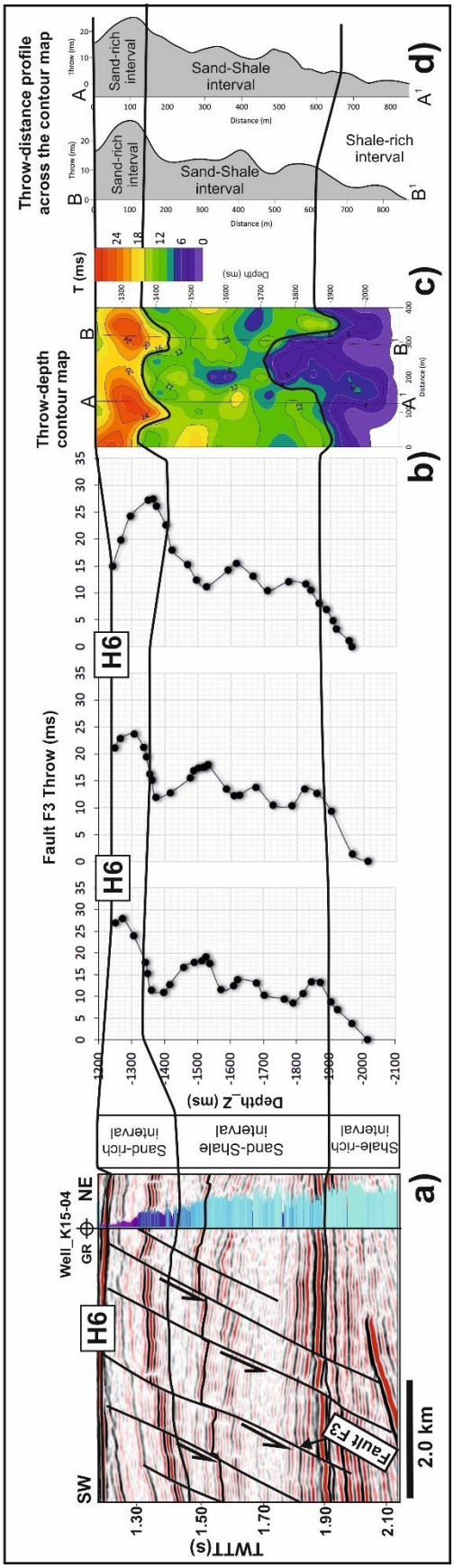
Correlation panel amongst fault throw distribution, lithology, and growth history for fault F3
a)
b)
c)
d)
Well_K15-04
GR
NE
SW
H6
Fault F3
2.0 km
TWTT(s)
Depth_Z (ms)
Fault F3 Throw (ms)
Sand-rich interval
Sand-Shale interval
Shale-rich interval
Throw-depth contour map
Throw-distance profile across the contour map
T (ms)
Depth (ms)
Distance (m)
Throw (ms)

Fig. 17

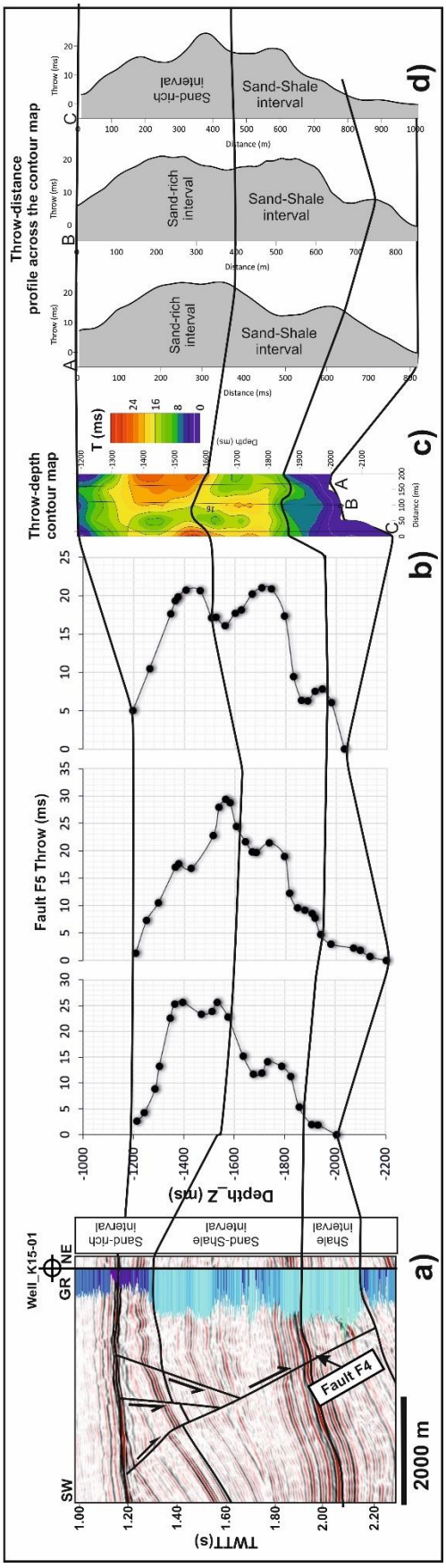
Correlation panel amongst fault throw distribution, lithology, and growth history for fault F4
a)
Well_K15-01
GR
NE
SW
Fault F4
2000 m
TWTT(s)
Shale interval
Sand-Shale interval
Sand-rich interval
Depth_Z (ms)
Fault F5 Throw (ms)
b)
Throw-depth contour map
T (ms)
Depth (ms)
Distance (ms)
c)
Throw-distance profile across the contour map
Throw (ms)
Distance (m)
Sand-rich interval
Sand-Shale interval
d)

Fig. 18

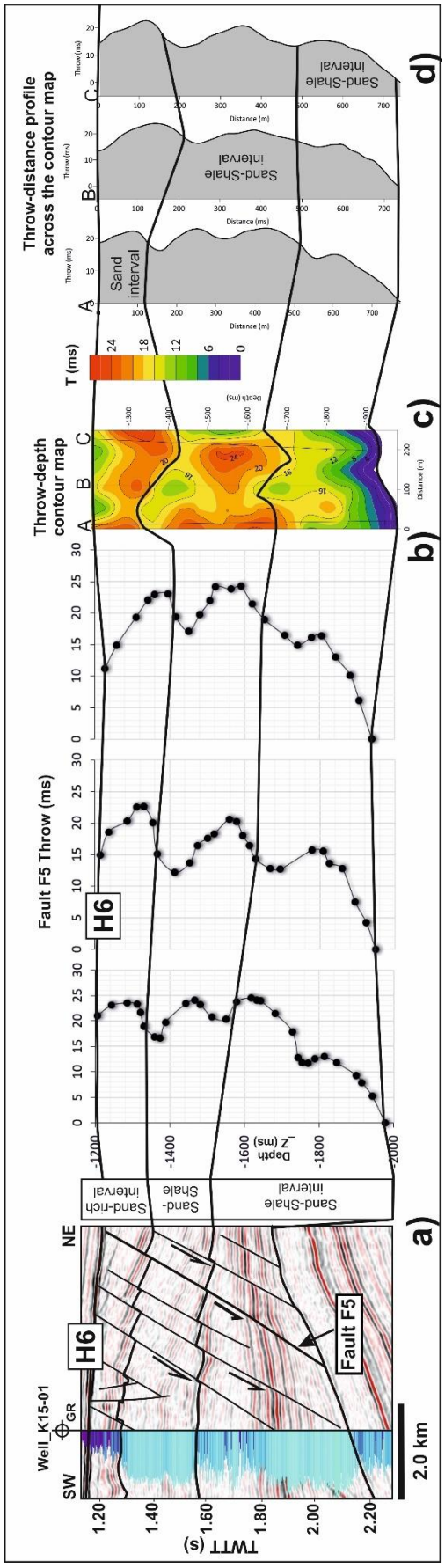
Correlation panel amongst fault throw distribution, lithology, and growth history for fault F5
Throw-distance profile across the contour map
Throw-depth contour map
Fault F5 Throw (ms)
Well_K15-01
GR
SW
NE
H6
Fault F5
Sand-Shale interval
Sand-rich interval
Sand-Shale interval
Sand interval
T (ms)
Depth (ms)
Distance (m)
Throw (ms)
TWTT (s)
2.0 km
a)
b)
c)
d)

Fig. 19

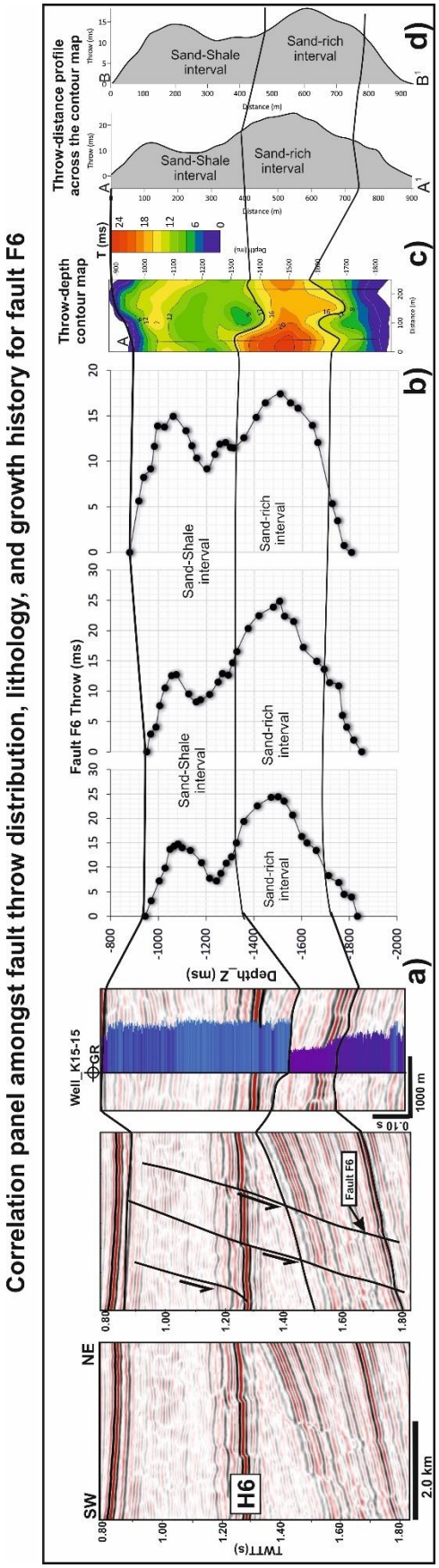
Correlation panel amongst fault throw distribution, lithology, and growth history for fault F6
a)
b)
c)
d)
Well_K15-15
GR
Depth_Z (ms)
TWTT(s)
NE
SW
H6
Fault F6
2.0 km
1000 m
0.10 s
Fault F6 Throw (ms)
Sand-Shale interval
Sand-rich interval
Throw-depth contour map
T (ms)
Depth (ms)
Throw-distance profile across the contour map
Throw (ms)
Distance (m)
A
A'
B
B'

Fig. 20

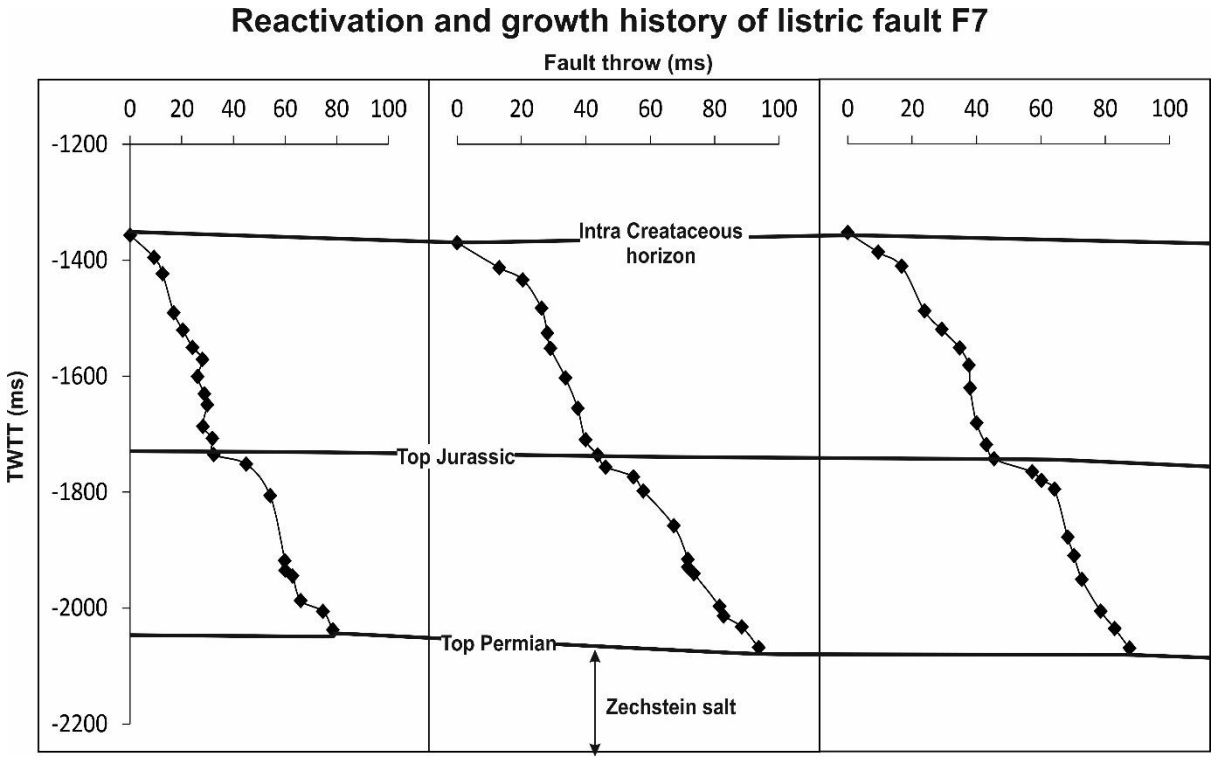
Reactivation and growth history of listric fault F7
Fault throw (ms)
0 20 40 60 80 100
0 20 40 60 80 100
0 20 40 60 80 100
TWTT (ms)
-1200
-1400
-1600
-1800
-2000
-2200
Intra Creataceous horizon
Top Jurassic
Top Permian
Zechstein salt

Fig. 21

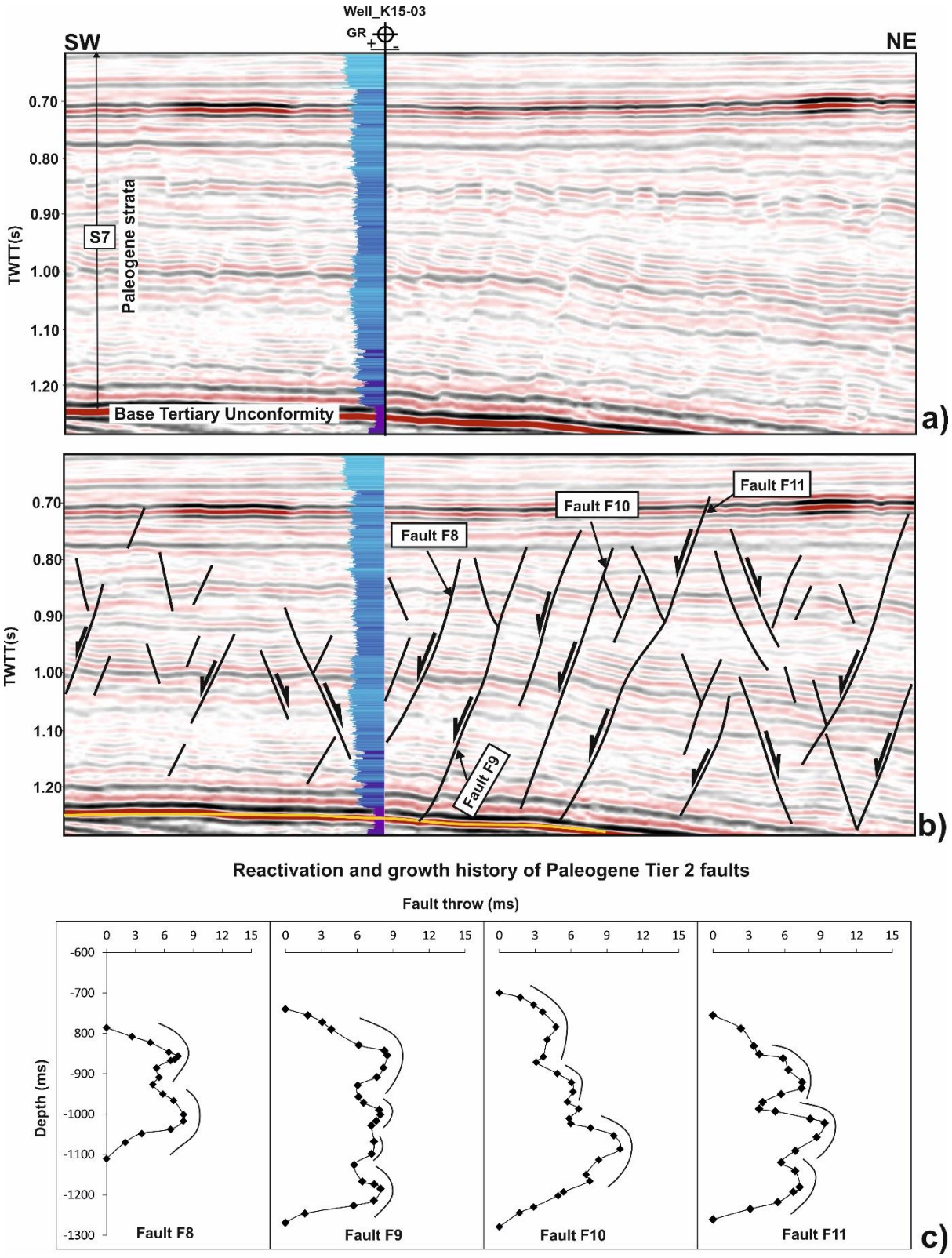
Well_K15-03
GR
SW
NE
TWTT(s)
0.70
0.80
0.90
1.00
1.10
1.20
S7
Paleogene strata
Base Tertiary Unconformity
a)
Fault F8
Fault F10
Fault F11
Fault F9
b)
Reactivation and growth history of Paleogene Tier 2 faults
Fault throw (ms)
0 3 6 9 12 15
Depth (ms)
-600
-700
-800
-900
-1000
-1100
-1200
-1300
Fault F8
Fault F9
Fault F10
Fault F11
c)

Fig. 22

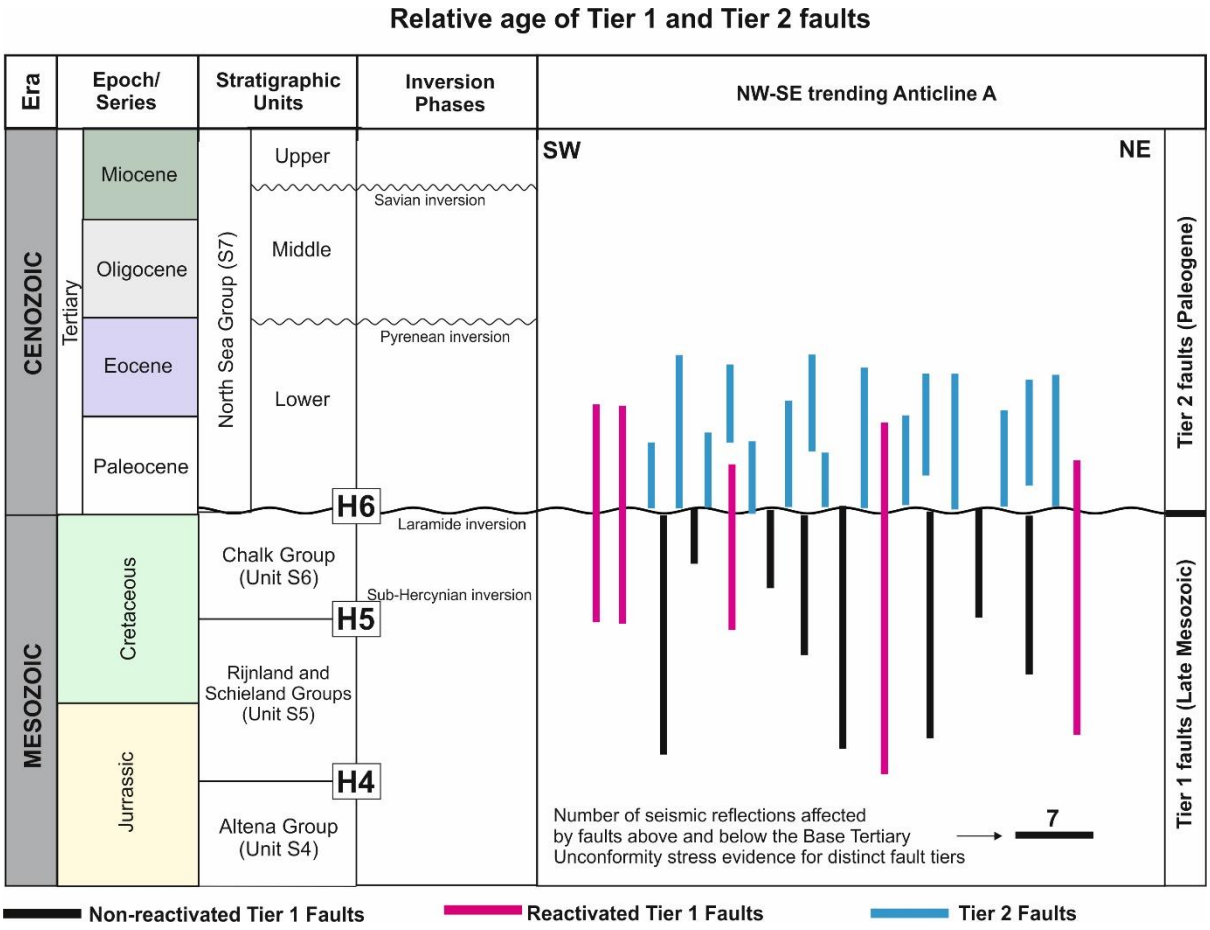
Relative age of Tier 1 and Tier 2 faults
Era
Epoch/ Series
Stratigraphic Units
Inversion Phases
NW-SE trending Anticline A
SW
NE
CENOZOIC
MESOZOIC
Tertiary
Miocene
Oligocene
Eocene
Paleocene
Cretaceous
Jurrassic
North Sea Group (S7)
Upper
Middle
Lower
Chalk Group (Unit S6)
Rijnland and Schieland Groups (Unit S5)
Altena Group (Unit S4)
Savian inversion
Pyrenean inversion
Laramide inversion
Sub-Hercynian inversion
H6
H5
H4
Tier 2 faults (Paleogene)
Tier 1 faults (Late Mesozoic)
Number of seismic reflections affected by faults above and below the Base Tertiary Unconformity stress evidence for distinct fault tiers
7
Non-reactivated Tier 1 Faults
Reactivated Tier 1 Faults
Tier 2 Faults

Fig. 23

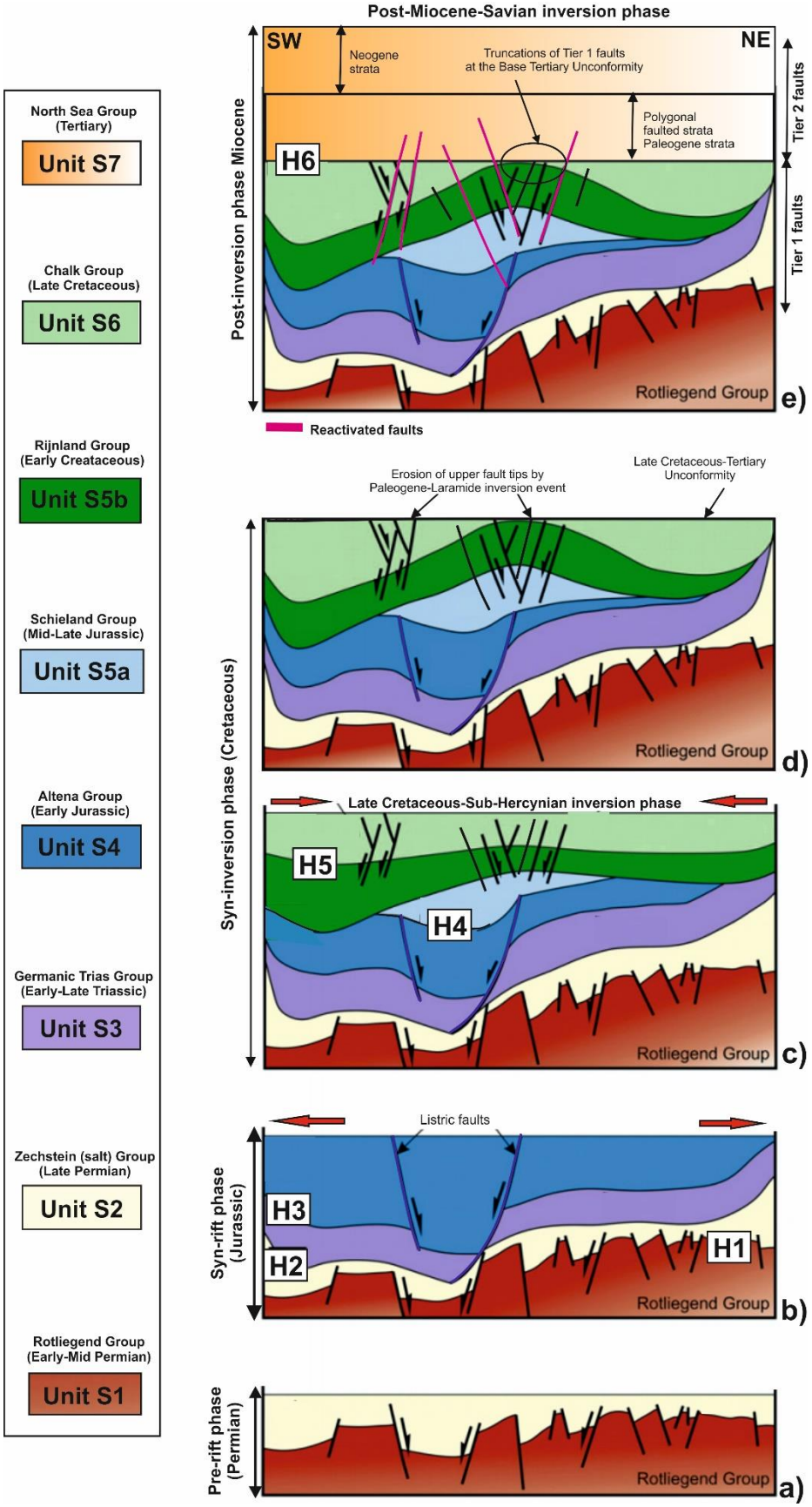
North Sea Group (Tertiary)
Unit S7
Chalk Group (Late Cretaceous)
Unit S6
Rijnland Group (Early Creataceous)
Unit S5b
Schieland Group (Mid-Late Jurassic)
Unit S5a
Altena Group (Early Jurassic)
Unit S4
Germanic Trias Group (Early-Late Triassic)
Unit S3
Zechstein (salt) Group (Late Permian)
Unit S2
Rotliegend Group (Early-Mid Permian)
Unit S1
Post-Miocene-Savian inversion phase
SW
NE
Neogene strata
Truncations of Tier 1 faults at the Base Tertiary Unconformity
Polygonal faulted strata Paleogene strata
Tier 2 faults
Tier 1 faults
Post-inversion phase Miocene
H6
Rotliegend Group
e)
Reactivated faults
Erosion of upper fault tips by Paleogene-Laramide inversion event
Late Cretaceous-Tertiary Unconformity
Syn-inversion phase (Cretaceous)
Rotliegend Group
d)
Late Cretaceous-Sub-Hercynian inversion phase
H5
H4
Rotliegend Group
c)
Listric faults
Syn-rift phase (Jurassic)
H3
H2
H1
Rotliegend Group
b)
Pre-rift phase (Permian)
Rotliegend Group
a)

Fig. 24

Table 1: Summary of principal features in the seismostratigraphic units of the Broad Fourteens Basin, Southern North Sea.

Seismic units	Stratigraphic Groups	Age of seismic units	Estimated Thickness (m)	Internal character of seismic units	Dominant lithologies (van Verweij and Simmelink, 2002)
Unit S7	North Sea Group	Paleocene to Recent	1,201	Characterised by a package of high-frequency, continuous and moderate to high-amplitude seismic reflections. Deformed by closely spaced polygonal normal faults.	Clays, sandstones, silts, locally gravel or peat, and brown coal seams.
Unit S6	Chalk Group	Late Cretaceous	684	Low amplitude and chaotic internal reflections. Erosion during the Laramide inversion event created a prominent Cretaceous-Tertiary boundary at the top of Chalk Group (H6). This boundary generated a strong, regionally mappable seismic reflector.	Limestones, marls, calcareous claystones and glauconitic sands
Unit S5	Rijnland and Schieland Groups	Late Jurassic to Early Cretaceous	505	Forms a package of high-amplitude, high-frequency seismic reflections. Deformed locally by closely spaced normal faults around the hinge region of Anticline A.	Carbonaceous claystones, marls and thick-bedded sandstones
Unit S4	Altena Group	Late Triassic to Middle Jurassic	259	Forms a package of high frequency, continuous and moderate to high-amplitude seismic reflections.	Argillaceous deposits, calcareous and clastic sediments. Bituminous Posidonia Shale Formation comprise the source interval for Jurassic oil plays
Unit S3	Germanic Trias Group	Early to Late Triassic	335	Forms a package with moderate frequency and moderate to high-amplitude seismic reflections. On seismic profiles, the bright reflection at the base of Germanic Trias Group (Unit S3) indicates a change from the high-velocity Zechstein salt (Unit S2) to the relatively low-velocity aeolian sandstones and lacustrine claystones of the Lower Germanic Trias Group.	Marine carbonates, evaporites. aeolian sands and lacustrine claystones. Aeolian sands and lacustrine claystones of the Lower Germanic Trias Group (the Buntsandstein Formation) form a prolific gas reservoir in the study area, particularly where Zechstein salt (Unit S2) has been withdrawn and welds have formed between Triassic (Unit S3) and the Rotliegend Group (Unit S1).
Unit S2	Zechstein Group	Late Permian	668	Low amplitude, chaotic internal reflections. The bright reflection at the top (H2) indicates a change from high-velocity Zechstein salt to relatively low-velocity aeolian sandstones and lacustrine claystones.	Thick layers of salt separated by cyclic carbonate intervals. Some of which are fragmented and deformed ('Stringers')
Unit S1	Rotliegend and Limburg Groups	Early to Middle Permian	690	Forms a package of moderate frequency and moderate amplitude seismic reflections. The base of the unit is hard to identify because the overlying salt dims the internal reflections of Rotliegend strata.	Terrestrial course grained sandstones (e.g. Slochteren Formation) and finer grained desert lake deposits (e.g. Silverpit Formation). Thick lacustrine and deltaic intervals with interbedded coal seams were deposited as part of the Limburg Group. Westphalian Coal Measures.